BIOSAT/PHI

BIOSphere-ATmosphere interaction mission/
Pointable Hyperspectral Imager

Full Proposal

in response to ESA's 2nd Call for Proposals for the

Earth Explorer Opportunity Missions

Reference Number: COM2-40

prepared by:

University of Wales Swansea (UK)
and
The BIOSAT Science Team

supported by:

SIRA Ltd. (UK)
Astrium Ltd. (UK)

Lead Investigator:

Prof. M.J. Barnsley,
University of Wales Swansea, UK

BIOSphere-ATmosphere interaction mission/Pointable Hyperspectral Imager (BIOSAT/PHI)

Executive Summary

Feedbacks between the land surface and the atmosphere are important determinants of the Earth's climate at a range of spatial and temporal scales. An enhanced understanding of the mechanisms involved would greatly improve the skill of climate model predictions and, hence, an assessment of the actual and potential effects of global climate change. Understanding the interactions between land-surface processes and climate oscillators, such as the El Niño Southern Oscillation and the North Atlantic Oscillation, is also of considerable importance. It would improve our ability to assess their likely impact, to develop improved land-management strategies to cope with their adverse impacts and to make maximum use of their beneficial effects.

The central rôle of Earth Observation in this context is to provide the dynamic, spatially-comprehensive data sets on the biosphere that are required by land-surface schemes (LSS) in Global and Regional Climate Models. Unfortunately, there are fundamental limitations to existing approaches to biophysical property retrieval from current satellite-sensor data. These primarily relate to the inability of broadband vegetation indices to distinguish the effects of variations in leaf/soil biochemistry from changes in vegetation canopy/soil surface structure. Hyperspectral imagers offer considerable potential for improved determination of surface biochemical properties, although this potential remains largely untapped from satellite-sensors. Similarly, information on surface structure can be obtained by inverting data from multiple-view-angle sensors against models of the surface Bidirectional Reflectance Distribution Function (BRDF). To date, however, the sensors used for this purpose have been coarse spatial resolution global imagers. This imposes limitations on the nature of the BRDF models that can be used owing to, among other things, issues of computational load and the spatial heterogeneity of the land surface. As a result, the relationships between the model parameters and the surface biophysical properties are uncertain.

The proposed solution is to combine a high spatial resolution, hyperspectral imager (PHI) with an agile satellite-platform (BIOSAT) capable observing a fixed target from multiple view directions both along- and across-track. This will make it possible to retrieve, simultaneously, information on the biochemical and structural properties of a range of surface materials and, hence, to provide the key parameter fields required as input to current and future generations of LSS. It will permit the inversion of physically-based BRDF models, for which the relationships between the model parameters and the corresponding surface biophysical properties are much better understood. Attention will be focused on test sites of environmental and climatological significance around the world. This will help to improve our understanding of the detailed feedback mechanisms involved between the land surface and climate, and to interpret and validate the results obtained from a range of global imaging satellite-sensors.

BIOSAT will be flown in a sun-synchronous, circular, near-polar orbit at a nominal altitude of $788km$, with an equator-crossing time of 9.30 hours. The platform will pitch and roll to provide pointing for the PHI instrument, in general allowing sets of images to be recorded for selected target areas at different along-track angles in each overpass. Pitch control will also provide moderate motion compensation, and roll will allow images to be recorded at a range of across-track angles from successive overpasses. The PHI instrument will be an imaging spectrometer operating in pushbroom imaging mode. It will cover the spectral range from $400nm$ to $1700nm$, using two detector types in a common spectrometer focal plane. The system will provide up to 120 readable spectral bands and will be programmable to optimize band selection for near-nadir and off-nadir images, and for different target requirements. The system will use on-board hardware for spectral calibration and relative response calibration, anchored by vicarious calibration. Moving parts will be avoided.

1 Scientific Justification

1.1 State of Scientific Knowledge

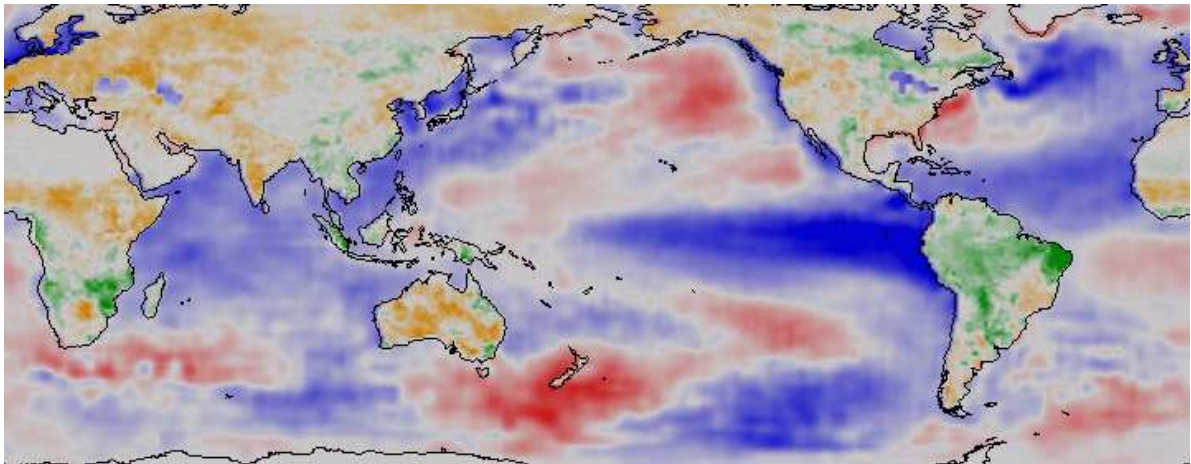### 1.1.1 Land-Surface–Climate Feedbacks

Feedbacks between the land surface and the atmosphere are important determinants of the Earth's climate at a range of spatial (local to global) and temporal (seasonal to decadal) scales. Pioneering work in this area was conducted by Charney, who demonstrated the potential rôle of vegetation removal in maintaining drought in sub-Saharan Africa (Charney *et al.* 1975). Many subsequent studies have also shown a sensitivity of climate — past (Otto-Bleisner and Upchurch 1997, Claussen and Gayler 1998), present (Xue and Shukla 1993, Polcher 1995) and future (Bounoua *et al.* 1999, Friedlingstein *et al.* 2001) — to both naturally- and anthropogenically-induced changes in land-surface properties.

Key properties involved in the feedbacks between the land surface and climate — *e.g.,* vegetation type and cover, soil moisture, and snow cover — evolve continuously in response to atmospheric/climatic forcing, although the initial forcing may be amplified or dampened as a consequence of their interaction (Delworth and Manabe 1993, Taylor and Lebel 1998, Koster *et al.* 2000). For example, Cox *et al.* (2000) suggest that dieback of the Amazonian rainforests over the next 50–100 years, in response to 'greenhouse' warming, may accelerate global climate change. Similarly, Zeng and others demonstrate the rôle of vegetation dynamics in enhancing regional climate variability at inter-annual to inter-decadal time scales, while presenting evidence to suggest that soil moisture stress on vegetation may contribute to the persistence of regional droughts (Zeng *et al.* 1999, Zeng and Neelin 2000).

An enhanced understanding of these feedback mechanisms would greatly improve the skill of climate model predictions and, hence, the assessment of the actual and potential effects of global climate change. Of equal, if not greater, importance is an assessment of variations in land-surface properties/processes that are affected by climate oscillators, such as the El Niño Southern Oscillation (ENSO) and the North Atlantic Oscillation (NAO) (Figure 1). Since these oscillators have a degree of predictability, studying their interactions with land-surface processes and investigating the feedback mechanisms involved may improve our ability to assess their likely impact, perhaps months in advance. Recent studies also suggest that climate oscillators operating on different time-scales interfere with one another, enhancing or negating each other's effect over particular time intervals (Los *et al.* 2001). Understanding these interferences and interactions will assist in the development of improved land-management strategies to cope with their adverse impacts or, where possible, to make maximum use of their beneficial effects.

1.1.2 Representation of Land-Surface–Climate Feedbacks in GCMs

Variations in energy and water balances, and in the transfer of mass and momentum, between the land surface and the atmosphere are represented by Land Surface Schemes (LSS) in Global Climate Models (GCMs) and Numerical Weather Prediction (NWP) models (Sellers 1986, Dickinson *et al.* 1998). LSS are regulated by a set of inter-dependent biophysical parameters, the values of which have traditionally been driven by prescribed land-cover classifications based on atlases and information published in the ecological literature (Matthews 1983). These essentially static parameterizations are unable, however, to account fully for the spatial and temporal variability inherent in the surface properties that they purport to represent (Sellers *et al.* 1996). To overcome this, global satellite-sensor data have been used to provide more explicit information on the spatial and tem-

(a) January 1983 (La Niña)
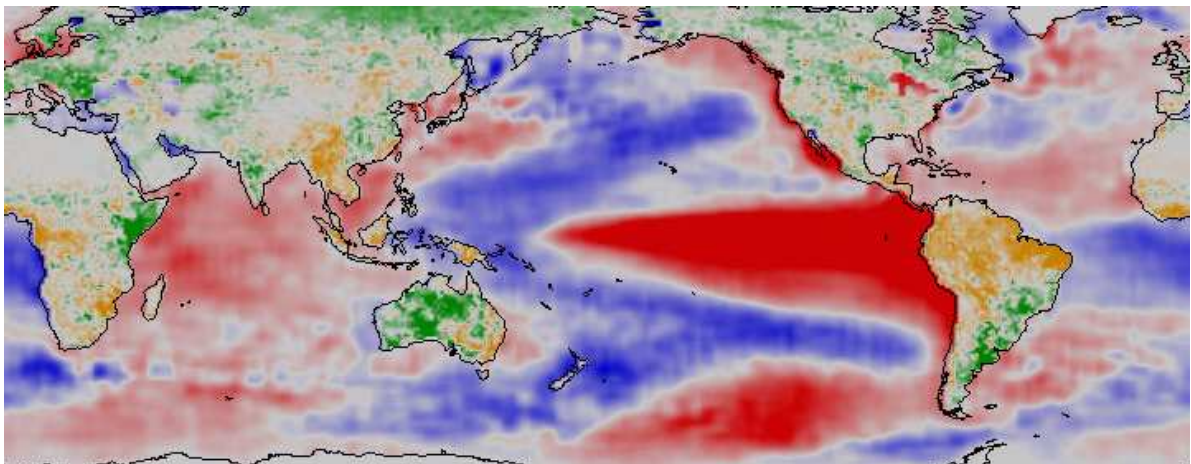
(b) January 1986 (El Niño)

Figure 1: Evidence of feedback between climate and the land-surface. Figures show anomalies in vegetation greenness (FASIR-NDVI; green=positive anomaly, brown=negative anomaly) and sea-surface temperature (red=positive, blue=negative) in (a) a La Niña year and (b) an El Niño year (after Los *et al.* 2001). Note the contrasting regional responses of vegetation to these climatic oscillators in the Amazon basin and, for example, equatorial Africa, Argentina and western Australia.

poral dynamics of vegetation (Defries *et al.* 1995, Sellers *et al.* 1996), while the latest generation of LSS simulate plant growth and competition interactively, and update the related land-surface properties accordingly (Foley *et al.* 1994, Dickinson *et al.* 1998). As a result, they seem to be able to simulate the overall carbon budget and the broad distribution of biomes across the globe. Despite this, considerable uncertainties remain, particularly in terms of respiration and soil water storage (Knorr and Heimann 2001). Enhancements are also required to improve LSS simulation of spatial heterogeneity and of interannual and regional vegetation patterns.

1.1.3   The Rôle of Satellite Remote Sensing and Considerations of Sub-Grid Scale Effects

One way to improve the representation of land-surface properties in existing LSS, including carbon cycle models, is to employ image data from Earth Observation (EO) sensors (Potter *et al.* 1993, Cayrol *et al.* 2000). These produce spatially comprehensive (m–km) and temporally explicit (daily–seasonal) information on the biosphere (*e.g.,* vegetation type, cover/amount, phenology and, potentially, soil water content) that can be incorporated into LSS by means of initialization, forcing, evaluation or assimilation (Knorr and Schulz 2001). Moreover, the archive of EO data is now long enough to detect interannual cycles/trends in the global biosphere (Los *et al.* 2000).

The use of remotely-sensed data within LSS has been made possible by increases in the computational power available to climate modelling. This has allowed the specification of finer spatial grids, in both GCMs and Regional Climate Models (RCMs), that are appropriate to an analysis of land-surface processes under changing environmental and climatic conditions. As a result, there is an increasing awareness of the sensitivity of spatially-averaged meteorological parameters to sub-grid-scale land-surface variability and of the need to incorporate such variability within climate models to improve seasonal to interannual forecasting (Cox *et al.* 1999). Indeed, a new generation of LSS has recently been developed that accounts for mixtures of vegetation types within a single grid box and that allows these components to interact with the overlying atmosphere (Cox *et al.* 1998, Koster *et al.* 2000). Although relatively crude at present, these models provide a framework for a more explicit description of sub-grid scale variability and feedback.

Importantly, these advances in climate modelling have been matched by developments in both the science and technology of Earth Observation. Specifically, the latest generation of satellite sensors are starting to produce data that are better calibrated (critical for long-term studies of subtle, but important, environmental changes), are more accurately geo-referenced, have finer spectral resolution and, hence, are more appropriate to the needs of the climate modelling community. At the same time, improvements in our understanding of, and ability to model, the physics of radiation transfer at the Earth surface mean that we are now better able to convert remotely-sensed measurements of surface-leaving radiance into accurate estimates of climatologically-significant land-surface properties or to assimilate them directly into LSS, where required.

1.1.4   Traditional Approaches to Deriving Land-Surface Properties from Remotely-Sensed Data

Previous studies suggest that satellite remote sensing has the potential to provide information on a range of *state* and *rate* variables/parameters required to initialize, force or evaluate LSS, or to be assimilated within them. These include measures of leaf/canopy biochemistry (*e.g.,* chlorophyll and water content), vegetation amount/density (*e.g.,* fractional ground cover, Leaf Area Index (LAI) and above-ground biomass) and radiation interception (*e.g.,* the fraction of Absorbed Photosynthetically-Active Radiation (f_{APAR}) and canopy light-use efficiency) (Baret and Guyot 1991, Waltershea *et al.* 1992, Leeuwen *et al.* 1994, Myneni and Williams 1994, Decolstoun *et al.* 1995, Roujean and Bréon 1995, Begue and Myneni 1996, Waltershea *et al.* 1997, Bar-

ton and North 2001). Estimation of these properties has traditionally been founded on the use of simple combinations of data recorded in relatively broad spectral wavebands centred on visible red and near-infrared (NIR) wavelengths — commonly known as vegetation indices (VIs) — by nadir-pointing sensors. These rely on the positive, asymptotic relationship that often exists between many vegetation canopy properties and total canopy reflectance at NIR wavelengths, and the corresponding negative, asymptotic relationship at red wavelengths. By taking a ratio of red and NIR reflectances, VIs seek to establish a relationship between the value of the index and the surface property while, at the same time, minimizing the influence of extraneous factors, such as variations in soil brightness (Qi *et al.* 1994), terrain slope and aspect (Holben *et al.* 1986), and atmospheric effects (Kaufman and Tanré 1992).

The principal advantages of VIs are their conceptual and computational simplicity: these explain their enduring attraction, despite their well-known limitations (Myneni *et al.* 1995, Verstraete *et al.* 1996). Specifically, broadband measurements of reflected radiance from soils and vegetation canopies are a composite function of three main factors, namely: 1) leaf and/or soil biochemistry; 2) vegetation amount and density/clumping; and 3) vegetation canopy architecture and/or soil surface structure. Unfortunately, most VIs lack an explicit mechanism to distinguish — and, hence, account for — the relative contributions of these three factors to the total surface-leaving radiance. This explains why VIs must normally be 'tuned' (calibrated) for data acquired by different sensors, over different vegetation types, or at different times of day/year (Verstraete *et al.* 1996). In other words, whenever the contributions due to the three factors changes (*e.g.,* because of a change of vegetation type, phenological effects or other environmental influence), the form of the relationship between the VI and the property of interest also alters.

1.1.5 The Rôle of Hyperspectral Imagers

One solution to the challenges outlined in §1.1.4, above, is to employ sensors that record data in a greater number of narrower spectral channels; that is, to use 'superspectral' or 'hyperspectral' instruments, as opposed to multispectral devices. Careful selection of the most appropriate spectral channels can help to minimize the impact of undesired environmental influences, while providing important information on key biochemical properties of the surface materials.

Peñuelas and others have, for example, demonstrated the use of narrow spectral wavebands in the red and NIR to estimate plant chlorophyll content, water status and biomass (Peñuelas *et al.* 1993, Filella and Peñuelas 1994, Peñuelas *et al.* 1996). It is common in such studies to calculate the first derivative of the detected spectral reflectance curve to derive estimates of the desired canopy biochemical properties. Particular attention is often given to the so-called 'Red-Edge Position' (REP) — the point of inflection on the spectral reflectance curve for vegetation between the local minimum at $\sim 680nm$ and the local maximum at $\sim 800nm$ — which appears to be a good indicator of changes in leaf and canopy biochemistry, most notably chlorophyll content (Boochs *et al.* 1990, Curran *et al.* 1995, Pinar and Curran 1996). To date, however, most REP studies have been carried out on carefully controlled, single-species vegetation canopies. Unfortunately, there is strong evidence to suggest that changes in canopy structure (*e.g.,* leaf wilt) and other confounding factors (*e.g.,* spatial variations in ground cover/LAI, vegetation type and soil substrate) place limits on simple, operational application of this technique to data from spaceborne sensors.
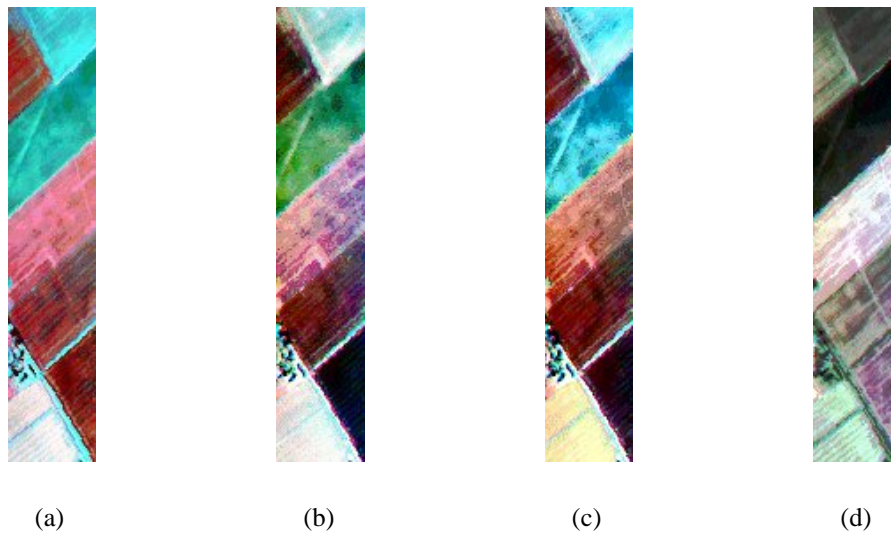
(a) (b) (c) (d)

Figure 2: (a) Standard, nadir-viewing, multispectral false-colour composite (NIR, red, green); (b)–(d) false-colour composite images generated using data recorded in a single spectral waveband (b = green; c = red; d = NIR), but at three different view angles with respect to the ground — two from opposing oblique angles and one close to nadir. In (a) the fields shown as red are cereal crops (wheat and barley), those shown as cyan are bare soil, while those shown as pink are oil seed rape. The same fields are shown in (b)–(d).

1.1.6 *Use of Multi-Angle Image Data to Determine Canopy/Soil Surface Structure*

The problem identified in §1.1.5, above, essentially distills down to the need for an independent assessment of the three-dimensional structure of the vegetation canopy and/or the soil substrate. This includes, but is not limited to, an evaluation of the fraction of ground covered by vegetation and its spatial distribution (*i.e.,* clumping) within each image pixel, as well as the size, shape, orientation and location of the plant elements (*e.g.,* leaves, stems, stalks, branches and flowers) within the vegetation canopy and the surface roughness of the soil below. In principle, bulk information on these properties for the vegetation canopy or soil surface as a whole can be obtained from an analysis of its directional (or angular) reflectance characteristics; in other words, by measuring the apparent reflectance at different sensor-view angles and solar-illumination angles (Barnsley 1994).

Clear visual evidence for the link between surface structure and directional reflectance is shown in Figure 2. This presents a comparison between a standard (multispectral) false-colour composite (FCC) image (Figure 2a) for an area of arable farmland and three FCC images of the same area (Figures 2b–d), each of which has been generated using data recorded in a *single* spectral waveband, but at three different view angles — two from opposing oblique angles and one close to nadir (Barnsley *et al.* 1997a). These are referred to as Multiple-View-Angle (MVA) images.

It should be evident from Figure 2 that the ability to distinguish the different surface materials is *at least* as good in the MVA images as in the multispectral FCC. In terms of the MVA images, this is because each surface scatters incident solar radiation anisotropically, and the nature of this anisotropy is largely dependent on the 3-D geometric structure of the reflecting surface. Thus, the relatively smooth exposed soils tend to exhibit strong forward scattering (and hence, for example, appear blue in Figure 2c), while the relatively rough cereal crops tend to exhibit stronger

backscattering (and hence, for example, appear red in Figure 2c).

A complete description of the directional reflectance properties of a surface, for all possible viewing and illumination angles, is given by the Bidirectional Reflectance Distribution Function (BRDF). Unfortunately, the BRDF cannot be measured directly, not least because it is defined in terms of infinitessimal elements of solid angle (Nicodemus *et al.* 1977). It can, however, be represented by a mathematical model, and many such models have been developed over the last 30 years (Goel 1987, Pinty and Verstraete 1992). If the model is founded in the physics of shortwave radiation transport and specified in terms of measurable biophysical properties, it is often possible to invert measurements of directional reflectance, sampled under a limited number of different Sun-target-sensor geometries, against the model — using numerical or analytical techniques — to yield estimates of the driving variables (*i.e.,* the surface biophysical properties) (Goel 1989, Antyufeev and Marshak 1990, Wu and Strahler 1994, Privette *et al.* 1996b, Barnsley *et al.* 1997c, Gao and Lesht 1997, Qiu *et al.* 1998).

1.1.7 *Biophysical Property Estimation through BRDF Model Inversion*

BRDF model inversion techniques are currently being applied, semi-operationally, to estimate land-surface biophysical properties from data acquired by a number of current and recent satellite sensors, including NOAA/AVHRR (Privette *et al.* 1996a), ADEOS/POLDER (Deschamps *et al.* 1994, Roujean *et al.* 1997), ERS/ATSR (Flowerdew and Haigh 1997), Terra/MODIS and Terra/MISR (Wanner *et al.* 1997, Justice *et al.* 1998, Strahler *et al.* 1999). The common characteristics are that (i) all are relatively coarse spatial resolution sensors ($\sim 1km$; $\sim 7km$ for POLDER) and (ii) the intention is to derive global data sets. This raises a number of important problems:

1. Most BRDF models are based on the assumption of radiation scattering from a homogeneous surface, which is generally unsustainable at the $1km$ grid scale;

2. The numerical techniques used to solve the inversion problem are typically too demanding in computational terms for application at the global scale and are not very robust to the initial estimates of the model parameters, due to the non-linear nature of many BRDF models; and

3. Validation of the derived data-products is problematic given the difference in spatial scale between the image data and the corresponding *in situ* measurement devices.

The first two of these problems has forced a general retreat from the use of more complex, physically-based BRDF models. The third remains a continuing issue.

The practical solution adopted in most studies to issues 1. and 2., above, has been to 'linearize' (essentially, to simplify) the BRDF models employed (Roujean *et al.* 1992, Wanner *et al.* 1995). This has a number of attractive ramifactions, including implicit modelling of spatial heterogeneity and the ability to derive fast, analytical solutions to the model inversion problem. Unfortunately, the model abstraction performed during the linearization process makes the relationship between many of the derived model parameters and the corresponding surface properties unreliable, except perhaps close to the point in parameter space where the linearization was performed. In short, while one may be able to *describe* adequately the directional reflectance properties of the land surface with such models, the relationships between the model outputs and the biophysical quantities of interest are much more problematic (Barnsley *et al.* 2000).

1.1.8   Review of Scientific Imperatives and Proposed Technical Solution

The preceding sections have outlined the current state of scientific knowledge in respect of feedbacks between the Earth's land surface and climate, and the representation of these through the use of Land Surface Schemes (LSS) within Global and Regional Climate Models. The ability to understand and to model these feedback mechanisms is vital to an improved understanding of climate change and, more specifically, of enhanced climatic variability, particularly at the regional scale. This entails a number of scientific challenges (IPCC 2001, Parry 2000), notably the need to:

1. Improve the representation of sub-grid scale land-surface processes in current LSS to enhance the skill of GCM/RCM predictions of future climate change;

2. Improve the understanding and representation of feedback mechanisms that enhance or suppress the effects of climatic oscillators (*e.g.,* ENSO and NAO) on land-surface processes;

3. Achieve tighter coupling of explicit hydrological and ecological sub-models within LSS, since most are currently designed for hydrological or ecological use, but not both;

4. Understand the causes of, and hence to resolve, inconsistencies between modelled and observed climates, particularly in terms of the spatial patterns of vegetation they produce; and

5. Understand and predict the regional consequences of climate and environmental change at the global scale, including climate variability.

The critical rôle of satellite remote sensing in this context is to provide the dynamic, internally-consistent and spatially-comprehensive information on the biosphere required by current LSS, through model initialization, forcing, evaluation and assimilation. The preceding sections have, however, highlighted the fundamental limitations of traditional approaches to biophysical property retrieval from satellite-sensor data. These centre on the inability of broadband vegetation indices to distinguish uniquely the effects of variations in leaf and soil biochemistry from changes in vegetation canopy and soil surface structure. It has been shown that hyperspectral imagers offer considerable potential for improved determination of surface biochemical properties, although this potential remains largely untapped from satellite-based sensors. Similarly, information on surface biophysical structure can be obtained by inverting data from multiple-view-angle sensors against appropriate models of the surface Bidirectional Reflectance Distribution Function (BRDF). To date, however, the sensors used for this purpose have been coarse spatial resolution global imagers. This imposes important limitations on the nature of the BRDF models that can be used due to, among other things, issues of computational load and considerations of the spatial heterogeneity of the land surface. As a consequence, the relationships between the derived model parameters and the surface biophysical properties of interest are, at best, uncertain.

The proposed solution to the technical and scientific problems outlined above is to combine a high spatial resolution, hyperspectral imager (PHI), capable of resolving in fine spectral detail the reflectance properties of Earth surface materials, with an agile satellite-platform (BIOSAT), capable observing a fixed target from multiple view directions both along- and across-track. In doing so, it will be possible to retrieve simultaneously information on the biochemical and biophysical (structural) properties of a range of Earth surface materials and, hence, to provide key parameter fields required as input to current and future generations of LSS (Verhoef 2000). The detailed technical characteristics of this mission are given in §2, but an important aspect of the

proposed mission, in addition to those outlined above, is its high spatial resolution. This will permit the inversion of more complex, physically-based BRDF models, for which the relationship between the retrieved model parameters and the corresponding surface biophysical properties is much better characterized and understood. Focusing on key sites of environmental and climatological significance around the world, this will not only help to improve our understanding of the detailed feedback mechanisms involved between the land surface and climate, but will also help to interpret and validate the results obtained from a whole suite of global imaging satellite-sensors.

1.1.9 Science Team

The mission demands a wide range of expertise to address each of the scientific and technical issues. To this end, we have brought together a carefully selected team of acknowledged international experts from a number of different fields, including the development of land-surface schemes for climate modelling (Harding), carbon cycle modelling (Kaduk), BRDF modelling and hyperspectral imaging (Barnsley, Jacquemoud, Lewis, Lucht, Privette), global vegetation dynamics (Los), plant physiology (Collatz), surface radiation fluxes (Dolman) and data assimilation (Kleidon). Full details are provided in the Annex.

1.2 Relevance of the Mission to the Earth Explorer Programme

This mission is relevant to three of the four science themes that ESA identified in its Living Planet programme. Theme 2 (Physical Climate) identifies the need for improved understanding of the interactions between ecosystems and climate, and the response of the land surface to climate changes. Land surface processes are important determining factors for long-term climate trends, but are not sufficiently well represented in climate models for their long-term evolution to be predicted confidently. Theme 3 (Geosphere-Biosphere) is probably the one most directly addressed by this mission. The measurements made, and the corresponding modelling activities, are immediately relevant to improved understanding, across a range of scales, of the energy and water cycles, ecosystem productivity, and the effects of land use change. The Living Planet definition of Theme 4 (Anthropogenic Change) has a clear bias towards atmospheric science, but it must be remembered that the land surface is where people actually live, and the effects of changes in atmospheric composition, pollution and resource depletion are all manifest on the habitable part of the globe. It is therefore vital to understand and quantify the responses of ecosystems to environmental disturbance, and to assess their resilience to anthropogenic change.

1.3 Relevance to other Programmes, Global Interests and Regional Needs

The mission will be relevant to intensive, large-area international field campaigns such as those coordinated by GEWEX and IGBP by providing high spectral, high temporal, multi-angle data for the regions that have been selected for enhanced observations. For example, data will be made available to investigators in field campaigns similar to FIFE, BOREAS, BALTEX, LBA or the Coordinated Enhance Observing Period (CEOP) initiative which is planned for 2002-2007 (Leese 2001) to aid the development of LSSs and carbon models tested during these campaigns. The collection of several years of data for these sites of interest would also aid the assessment of the effects of climate on vegetation and *vice versa,* and would link in with initiatives such as CLIVAR.

The ability to use the high resolution, hyperspectral data to simulate various sensors under various illumination conditions will aid the cross-calibration of data from previous-generation sensors, such as NOAA/AVHRR, and the newer types of sensors, such as ENVISAT, MODIS, POLDER

and VEGETATION. This would aid the continuation of the time-series data sets started using data from the earlier satellite-sensors, with important benefits for programmes such as the ISLSCP initiative I and II. These linkages will greatly enhance the benefit of the BIOSAT/PHI mission.

2 General Mission Characteristics

2.1 Scientific and Technical Requirements

The scientific objectives set out in §1 demand a novel type of mission. The objectives address issues of global concern, but the most pressing need is not for the generation of yet more global data sets, or even better global models. Global models can already be fed by data sets from missions such as Envisat and Terra. These deliver spatially-aggregated ('lumped') radiances at kilometric scales, for which most areas areas of the Earth surface must be considered to be spatially heterogeneous. Proper interpretation of radiation reflected from such composite ('mixed') pixels requires measurement and modelling at much finer spatial scales. This mission delivers the data needed to initialize, force, validate and assimilate within LSS at the relevant scale *i.e.,* to feed the detailed understanding of the functioning of vegetation, and its evolution in response to environmental and climatic perturbation, at the level of basic landscape units.

Instead of attempting to collect data over the whole land surface and deliver global sets of geophysical parameters, we will make frequent observations at high spatial resolution over a just a small proportion of the land surface, but in areas that are representative of the full range of significant biomes and landscapes. Most of the areas imaged will be centred on experimental test sites set up under a variety of national and international programmes to study specific science questions, such as hydrological processes at regional and sub-GCM scales.

The mission needs, as we shall see, not only to have high spatial and temporal resolutions, but also to capture data directionally, and in a large number of spectral channels. Above all, it needs to retain a great deal of flexibility in the way the main instrument is deployed. The preferred realisation for the mission is an imaging spectrometer, flown on an agile, pointable platform. Our heritage for this concept is the current CHRIS/PROBA mission.

We expect that there will be two approaches to the use of the data in the lifetime of this mission. The first is currently more widely used in vegetation modelling, and consists of estimating appropriate parameters and using spatially explicit fields of these parameters in distributed LSS and other models. The second, which is increasing in importance, is the direct of assimilation of top-of-canopy radiance data into dynamic models of vegetation growth.

2.2 Mission Duration, Timing Requirements, Relation/Dependence on other Missions

2.2.1 Mission Duration

The scientific objectives of the mission are centred on a study of the seasonal and inter-annual responses of the land surface to climatological forcing. In this context, Los *et al.* (2001) have shown that anomalies in vegetation greenness, sea-surface temperature (SST), land-surface air-temperature and precipitation at the global scale exhibit linked, low-frequency, inter-annual variations with dominant periods of about 2.6 and 3.4 years. The former are thought to be associated with variations in the ENSO index and the latter to variations in NAO index. To be assured of sampling at least one full ENSO/NAO cycle, therefore, a mission duration of five years is required.

Table 1: Geophysical data products.

Property	VIS	NIR	SWIR
Albedo (spectral and broadband)	●	●	●
Fraction of Absorbed Photosynthetically-Active Radiation (fAPAR)	●	●	
Leaf Area Index (LAI)	●	●	
Fractional ground cover of vegetation	●	●	
Above-ground biomass (green and sensecent)	●	●	●
Canopy/leaf chlorophyll content	●	●	
Canopy/leaf water content		●	●
Phytophenology (date of onset and duration of growing season)	●	●	●
Land cover type/plant functional type	●	●	●
Vegetation canopy structure	●	●	●

2.2.2 Timing Requirements

There are no specific timing requirements involved in this mission, other than the five-year lifetime. The mission will, however, benefit from overlap with other, coarser spatial resolution satellite sensor missions (*e.g.,* Envisat). Simultaneous acquisition of multi-angle, high spatial and spectral resolution image data from BIOSAT/PHI and coarse spatial resolution data from one or more global imagers would enable cross-calibration of these instruments and a greater understanding of the effects of spatial scaling inherent in the data acquired by coarser resolution sensors.

2.2.3 Relation/Dependence on Other Missions

BIOSAT/PHI has no critical dependence on other satellite-sensor missions. Nevertheless, significant benefits will accrue from near-simultaneous data acquisition with other satellite sensors (*e.g.,* Envisat/MERIS and the MODIS and MISR instruments on board Terra, and their successors) over selected target sites. As noted in §1.1.8 and §2.2.2, above, this would allow cross-calibration, validation and spatial scaling studies to be performed, that would enhance the value of data from each of the missions concerned. Should SPECTRA be launched as part of ESA's Earth Explorer Core Mission, there will be important opportunities for synergy with BIOSAT/PHI. Assuming that the two satellites share similar, but out-of-phase orbits, it will be possible to increase greatly the number and angular range of directional reflectance samples for a given target area. This would yield still more accurate estimates of the surface biophysical and biochemical properties.

2.3 Geophysical Data Products and Retrieval Algorithms

2.3.1 Geophysical Data Products

Table 1 lists the primary geophysical data products that will be generated from BIOSAT/PHI, together with the relevant regions of the electromagnetic spectrum within which measurements must be made to deliver them. The data products selected describe a wide range of properties pertaining to the biosphere, notably the type, biochemical properties, spatial distribution, density/amount, $3D$ structure and temporal/dynamic characteristics of vegetation. They represent products that can readily be incorporated into LSS through model initialization, forcing, evaluation or asimilation.

2.3.2 Retrieval Algorithms

The methods used to retrieve the geophysical parameters listed in Table 1 will build on the heritage of algorithms developed for current airborne- and satellite-sensor missions. For example, there has been considerable development of BRDF model inversion algorithms for albedo, LAI/biomass and fAPAR estimation in recent years, driven largely by the needs of NASA's MISR and MODIS missions (Diner *et al.* 1998, Strahler *et al.* 1999). In view of the high spatial resolution of the BIOSAT/PHI mission, however, it will be possible to exploit more complex BRDF models (*i.e.,* ones based more closely on the physics of shortwave radiation transport), for the reasons outlined in §1.1.7. Look-Up Table (LUT) approaches to model inversion will be employed to avoid the problems associated with standard, numerical inversion routines (Barnsley *et al.* 2000).

Estimation of fractional ground cover can be achieved using a range of algorithms, including mixture-modelling methods (Ichoku and Karnieli 1996). Similarly, it will be relatively straightforward to apply existing algorithms for hyperspectral data analysis, such as REP techniques to estimate leaf/canopy biochemistry and water content (Pinar and Curran 1996), to data from BIOSAT/PHI, but exciting, new opportunities exist for simultaneous retrieval of surface biochemical and biophysical properties based on spectral BRDF models. Finally, information on surface phytophenology (including the length of the growing season) and plant functional type will be retrieved through an analysis of the spatial and temporal profiles of the geophysical parameters discussed above.

The chief difficulty in quantitative use of optical data is correction for the unknown scattering by atmospheric aerosols. Multi-angular data offer the potential for improved correction for the effects of atmospheric scattering (Diner *et al.* 1998, North *et al.* 1999), allowing correction over regions where no appropriate spectral targets are available.

2.4 Observation Requirements

ESA has already commissioned several studies to define the observational requirements for a satellite mission that would be dedicated to monitoring land-surface processes. Those arguments have been well organised and are presented in documents prepared for the Granada meetings of October 1999 and October 2001. The studies emphasized the importance of making directional measurements, a fact that had been largely overlooked in previous land-surface missions. The requirements identified below naturally bear some similarity to those derived in that document, but there are certain, important differences. These arise from the desire to permit a more flexible observation pattern, based on a smaller number of sites that can, as a result, be imaged with higher frequency. This will permit compilation of comprehensive datasets of the BRDF for the world's major biomes.

2.4.1 Directional Requirements

Radiation reflected from natural surfaces is almost always anisotropic. Consequently, the signal recorded in a single direction will not usually enable one to make any statement with confidence about the surface radiation environment. On the other hand, if measurements are taken almost simultaneously at several different directions, preferably in or close to the solar principal plane (*i.e.,* the plane of the Sun), it is possible to obtain a more accurate estimate of the surface spectral albedo (Lucht *et al.* 2000) — a key parameter in studies of the net radiation balance at the Earth surface — as well as information on the mean structural properties of the soil surface or vegetation canopy (Verstraete *et al.* 1996). It is therefore proposed to acquire images from *at least* 5, and

preferably 7 or more, different view directions during a single overpass, using the same method (along-track pointing) as is employed by the CHRIS/PROBA system.

One of the most striking features of the distribution of directional reflectance from almost all natural surfaces illuminated by direct sunlight is the 'hot spot'. This is a local maximum of reflectance in the direction of solar illumination, caused by the absence of shadows thrown by the small-scale scatterers in the field-of-view. This feature is largely unimportant to determining the surface radiation budget, but its width and amplitude carry key information about the local structural properties of the canopy (Goel *et al.* 1997). It is therefore essential that BIOSAT/PHI is able to sample in this direction.

The pointing capability of BIOSAT/PHI will be deployed in three main modes of operation:

1. '*Standard*' mode. An image will be captured near-nadir, with other images being captured fore and aft of this position at matching zenith angles during a single orbital overpass, similar to the current CHRIS/PROBA system. The near-nadir image is needed to give the highest at-ground spatial resolution, which will enable the co-registration of both multi-angle and multi-temporal data at the experimental sites. The off-nadir pairs should probably not be acquired at zenith angles exceeding $60°$ (at ground), since the atmospheric path lengths become longer than the natural scale of aerosol concentration and the errors involved in atmospheric correction of the images become significant. On the other hand, the shape of the BRDF needs to be sampled at large angles, so we propose to elect $\pm60°$ as our most extreme pair. A second pair between $\pm45°$ and $\pm30°$ gives us five reasonably-spaced samples of the smooth 'bowl' shape of the surface reflectance distribution. The minimum of the bowl is usually found off-nadir on the opposite side to the hot-spot, at approximately the same zenith angle. It would be desirable to sample at, or close to, this direction. This implies a greater degree of flexibility in terms of pointing angles, since this position varies with the solar angle and, hence, with the latitude.

2. '*Fine sampling*' mode. This mode will provide images at a large number of view directions in a single overpass - provisionally up to 100 views at intervals down to $1°$. In this mode, the along-track size of the area imaged will be restricted to $< 10km$, to limit demands on the platform AOCS system. In general, the number of spectral bands read out at off-nadir angles may be reduced to limit data storage requirements. The intense sampling of the BRDF is a *unique* feature that will enable validation and refinement of radiative transfer models for complex, incomplete vegetation canopies, such models being required by the data assimilation schemes that are likely to be widely employed in the timeframe of this mission. These images need not be co-located with instrumented ground sites, as the richness of the spectro-directional data set will allow data-driven atmospheric corrections.

3. '*Hybrid*' mode. Images are acquired at nadir, $\pm60°$, $\pm45°$, at the bowl minimum and, for a reduced along-track image, around the hot spot with a reduced fine sampling operation sandwiched between the other views. This gives us the spectral albedo across the field-of-view, as well as the detailed structural information for a smaller sub-scene, which we can confidently locate within the bigger picture.

The most important overall condition is that the viewing geometry should be kept as flexible as possible. The directional requirements must **not** be 'hard-wired'. With the design of BIOSAT/PHI being based on our experiences with CHRIS/PROBA, we are limited only by the maximum torques that can be tolerated by the momentum wheels and the software needed to drive the pointing.

2.4.2 *Spatial Resolution Requirements*

Spatial Sampling Interval   Current understanding of land-surface–climate interactions is based on basic physical laws, coded into models of plant and canopy functioning, that have been validated by measurements typically made at a spatial scale of a few metres. On the other hand, the effects that we wish to understand occur at the scale of landscape units (kilometers to tens or hundreds of kilometers), whether these are forest fragments in Amazonia, intensively-farmed regions in Europe, or areas of sensitive, semi-natural vegetation in transition zones such as the Sahel. These two scales — the one at which we need to understand the climate feedbacks and the one at which we can validate our basic process models — need to be bridged by data collected at an intermediate scale. These data can be used, together with point-process studies, to initialize, force and evaluate the distributed models that are required to understand complex landscapes.

Choosing an appropriate sensor spatial resolution to meet this need is problematic, since no two landscape are alike. Neverthless, studies in the field of landscape ecology suggest that the spatial variability in most landscapes exhibits peaks at just a few scales (O'Neill *et al.* 1986). These mark transitions between so-called 'domains of scale' (Weins 1989), between which a single set of environmental processes dominates. Numerous studies have attempted to identify domains of scale in natural, semi-natural and managed landscapes, using digital remotely-sensed images and various measures of spatial variability. Scale variance analysis (Moellering and Tobler 1972) has been widely employed for this purpose. Figure 3 presents an example of scale variance analysis applied to a Landsat-TM sub-scene covering south-east England, taken from a study by Barnsley *et al.* (1997b). It illustrates that this complex landscape, which contains a mixture of large connurbations and various types of farmland, exhibits two peaks of spatial variation — one occurring at a scale of approximately 120–$240m$ (field-to-field variation), the other between 4–$8km$ (broader land-cover variations). Similar figures have, however, been reported for a range of other landscapes (Townshend and Justice 1988). Since we are interested in capturing sub-grid-scale variability in the context of LSS, we are primarily concerned with the finer of these two spatial scales. Thus, a spatial resolution of about $100m$ would seem to be an appropriate compromise. At resolutions much finer than this, the sensor will tend to over-sample the inherent spatial variability of the terrain (leading to unnecessarily increased data volumes); much coarser than this and the ground resolution elements ('pixels') will become mixed (heterogeneous). A spatial resolution of $100m$ is also workable in terms of *in situ* validation by point measurements.

It is important to recall that the data sets generated by BIOSAT/PHI will be multi-angular. It is an inescapable fact of geometry that the land area subtended off-nadir by a given solid angle is a different size and shape from that seen at nadir. For example, in the images acquired at $\pm60°$ the ground resolution element ('pixel size') will be four times larger along-track and twice as wide across-track as that of a nadir-viewing pixel. To avoid aliasing problems between images in a multi-angle set, all of the images will therefore need to be resampled to the spatial resolution of the coarsest image in the set (*i.e.,* the image acquired at the largest view angle). This means that if we wish to achieve a target spatial resolution of $100m$ for the largest off-nadir image, the spatial resolution at nadir will need to be between $25m$ and $50m$.

Swath   This mission is not intended to gather data for all points on the globe, but will concentrate instead on collecting detailed images for specific target areas in regions of climatological significance, such as areas of landscape disturbance (*e.g.,* deforestation or desertification). In this context, the extent of the complete data set should be such as could be handled confidently and accurately in, say, a regional hydrological model. A scale of a few tens of kilometres is suggested: this is
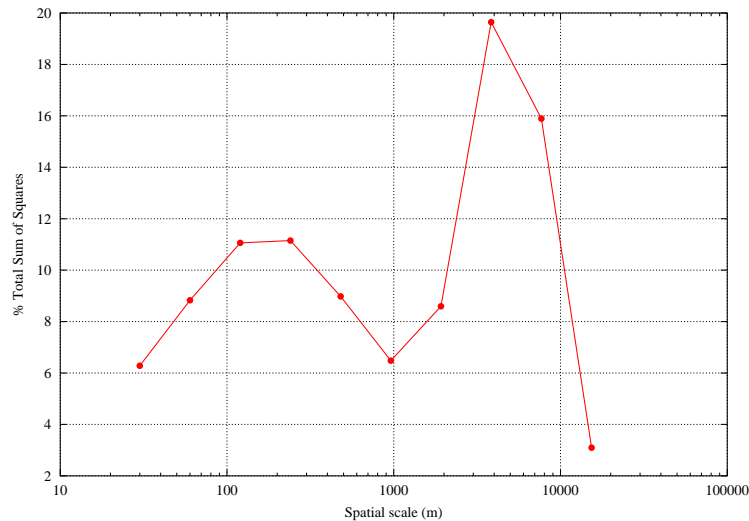
Figure 3: Results of scale variance analysis for a 2048×2048 pixel Landsat-TM sub-scene (NIR) covering part of south-east England (after Barnsley *et al.* 1997b).

about the size of a grid cell in current GCMs, and is not too large to be modelled meaningfully. Consequently, we have settled on $50km$ as the default swath width.

Spatial (Image-to-Image) Registration   To determine the directional reflectance signal of the land surface with confidence, it will be important to achieve accurate registration between each image in a multiple-view-angle data set. Mis-registration between images acquired over non-homogenous scenes induces a de-correlation effect that can be similar in magnitude and form to the directional reflectance signal that we wish to measure (Barnsley and Allison 1996). To overcome this we propose to employ a combination of accurate knowledge of the location and attitude of the satellite-platform in orbit and careful pre-processing of the resultant image data using image correlation techniques (see, for example, Barnsley *et al.* (1997c)) to achieve sub-pixel registration accuracy.

2.4.3   Temporal sampling requirements

A mission lifetime of five years is required, the scientific justification for which is given in §2.2.1. The other important aspect of temporal sampling relates to the frequency with which any given site can be imaged. Vegetation processes do not occur at a uniform rate and, during certain periods, the structural and functional condition of a canopy can remain virtually unchanged for months. At other times, however, important phytophenological changes occur on an almost daily basis, such that a revisit capability measured in weeks would be too long, leading to the very real danger of missing key episodic and seasonal events. Vegetation at higher latitudes, in particular, undergoes short periods of intense activity during spring (*i.e.,* the greening phase; see, for example, the period between mid-April and mid-May in Figure 4) and at the end of the season (*i.e.,* the senescence phase). At such times, it would be highly desirable to access the study area every two to three days. In the context of this mission, this is arguably more important than being able to revisit any point on the Earth surface in the minimum time possible. By acquiring data over a selected study site on several successive days, for example, one could construct a much more complete and consistent record of the surface BRDF than by collecting a single string of multi-angle data once every three days, since changes in the surface and the atmosphere would be kept to a minimum.
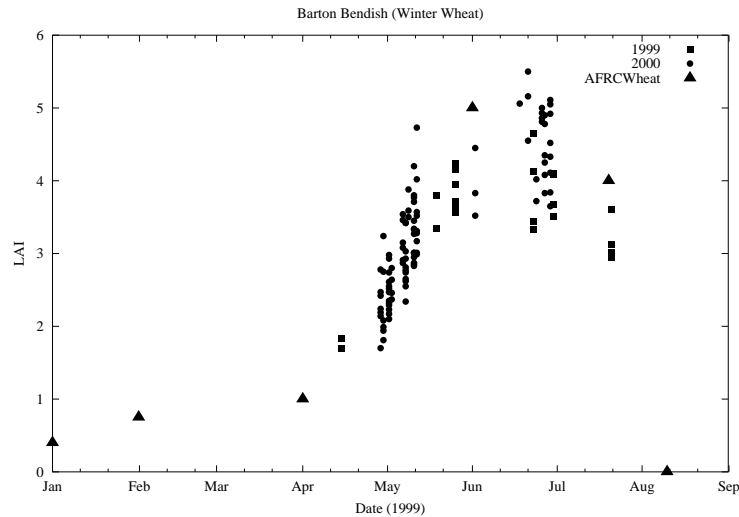
Figure 4: Temporal variations in ground-based measurements and plant-growth model simulations of LAI over a winter wheat crop in the UK.

The incidence of cloud cover complicates this requirement, albeit only slightly. This is because cloud cover is strongly correlated in temporal terms: cloudy days tend to come in sequences, such that if a site is clear on one overpass there is a good chance of clear conditions during the next overpass. The converse is also true, however.

2.4.4 Spectral Sampling Requirements

At the risk of over-simplifying the complex nature of surface reflection, one can say that directional variations in reflectance are broadly determined by surface (canopy) structure, while spectral (wavelength-dependent) variations in reflectance are primarily determined by biochemistry (*i.e.,* plant pigments, canopy water content, soil composition) (Asner 1998). Spectral variation in reflectance is also determined to some extent by structure, especially in the NIR (750–$900nm$).

Spectral Range The most important wavelength range for studying vegetation is the visible to NIR part of the spectrum, broadly speaking between $450nm$ and $900nm$ (hereafter referred to as spectral range A). The major part of the solar irradiance is contained in this region of the electromagnetic spectrum. Consequently, studies of the net radiation budget require this region to be covered with fairly high sampling density. Moreover, the most striking feature of vegetation reflectance spectra, the so-called 'red-edge', lies at the heart of this region. At wavelengths shorter than this narrow transition zone, vegetation absorbs almost all of the radiation incident upon it, whereas for most longer wavelengths it absorbs virtually none. The proportion of NIR radiation scattered and transmitted is, however, a function of canopy optical depth and vegetation health, so the full range of this wavelength region needs to be acquired. Not surprisingly, this wavelength range is covered by CHRIS/PROBA, as well as by most other airborne and hand-held spectroradiometers.

It is important, however, to extend the spectral range of BIOSAT/PHI to longer wavelengths as well, to cover the region between $900nm$ and $1700nm$ (hereafter referred to as spectral range B). In the first instance, a significant fraction of solar radiation lies at wavelengths longer than $900nm$, such that attempts to estimate albedo, or net shortwave radiation, using data from range A alone are liable to error. Furthermore, vegetation and soil spectra are very different in range B, and this

16

Table 2: Visibility of a typical site at $50°N$ from BIOSAT-PHI.

Day	1	2	3	4	5	6	7	8	9	10	11	12	13
Observed	●	●		●	●		●	●			●		

Day	14	15	16	17	18	19	20	21	22	23	24	25
Observed	●			●			●	●		●		

additional contrast is highly beneficial in inverting BRDF models. In addition, estimates of canopy water content, which are just possible using the wavelength range 0.9–$1.0\mu m$, are made much more robust by including further absorption features in range B. More speculatively, laboratory studies have suggested that it is possible to retrieve estimates of plant lignin and cellulose content using this spectral region (Curran *et al.* 1992), although this has yet to be achieved operationally. It is possible that part of the problem has been the confounding effects of canopy architecture (see §1.1.5). Directional observations in the shortwave infra-red, which are not currently available either from space or from aircraft, may help to resolve this. Both ranges A and B are needed to quantify the key biophysical and biochemical properties of ecosystem functioning (Table 1).

Spectral resolution   Estimates of plant chlorophyll concentration and leaf water content can be made from measurements provided the spectral resolution is sufficiently fine (Filella and Peñuelas 1994, Pinar and Curran 1996). These properties will be retrieved by fitting the observed data to theoretical/laboratory curves of the main absorption features of vegetation spectra. These tend to be of the order of 50–$70nm$ from maximum to minimum. At least three samples are required across the feature to ensure accurate retrieval, such that the spectral sampling interval should be no greater than 15–$20nm$. Retrieval accuracy is believed to be most sensitive at the red-edge (690–$750nm$), where the spectral sampling should be increased to five or six channels per feature. This implies better than $10nm$ sampling. In range B, the features are not well described from space, such that 15–$20nm$ sampling can be tolerated.

2.4.5   Orbit

BIOSAT will be injected into a circular $788km$ sun-synchronous orbit with an inclination of $98.60°$. This orbit will have a 25-day repeat cycle and a worst case revisit time of 5 days at the equator based on $30°$ across-track pointing. A relatively high orbit and equator crossing time of 09:30 have been selected to provide optimum viewing conditions, including sufficient time to acquire multiple-view-angle observations of a site within a single overpass. The resultant visibility of a typical site is shown in Table 2. A site at latitude $50°N$ is visible on 12 of the 25 days, but the acquisition opportunities are grouped, with six of them occurring within an 8-day period. The altitude and inclination angle of the orbit have been selected deliberately to bring this about. The grouping means that a maximum number of image sets of the target site can be acquired — each from a different view zenith angle and each at a slightly different solar elevation angle — over the course of just a few days. This allows a much more detailed representation of the surface BRDF (and, hence, of the surface structure) to be constructed than would be possible through a more even spacing of acquisitions (for which the same amount of data would take longer to collect, with the retrievals more likely to be confounded by changes at the surface or in the atmosphere).
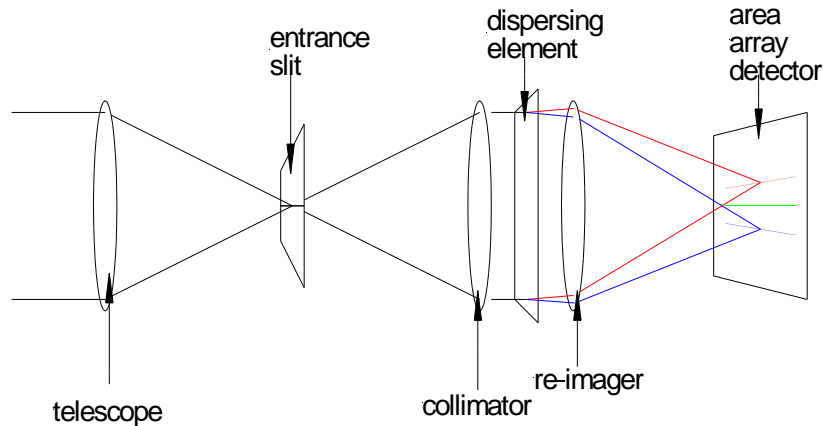
Figure 5: Schematic diagram of a conventional imaging spectrometer

2.4.6 Summary

To fulfill the scientific objectives of the mission, BIOSAT/PHI must be able to observe the Earth surface at a fine spatial resolution, with the capability to revisit a site as often as possible within a short period of time. A highly flexible pointing capability is required, with the ability to image across most of the range of reflected sunlight and to resolve this into a fine spectrum.

3 Technical Concept

The proposed mission requires an Earth-observing hyperspectral sensor, flown on an agile platform in a near-polar, low-Earth orbit. The sensor and platform are described in §3.1 and §3.2, the ground segment and data acquisition in §3.4, data processing and dissemination in §3.5, and §3.6 describes the proposed validation approach.

3.1 Sensor (PHI)

3.1.1 Optical design and methods

Basic imaging and spectral resolution methods   The instrument is an imaging spectrometer, operating in a conventional pushbroom imaging mode. Instantaneously, the telescope will image a line of resolved areas on the ground onto the spectrometer entrance slit, as indicated schematically in Figure 5. The spectrometer optics will re-image the strip of Earth onto an area-array detector, using refracting prisms to spread the spectrum of each image point spectrally in the direction orthogonal to the monochrome line-image. Thus, the strip of Earth will be imaged in each wavelength onto a row of detector pixels, and the spectrum of each point in the line will be imaged on a detector column. When read out, the image on the detector will provide detailed spectral data for each point in the line-image, giving the spectral coverage and resolution shown in Table 3.

The instantaneous line-field will be aligned nominally orthogonal to the platform motion, such that the platform motion will be used to scan the line-field over the Earth surface to record full spectral data for an area on the ground. The detector integration period (between each frame read) will generally be set approximately equal to the time taken to scan over the spatial resolution interval on the ground (nominally the width of the slit-image projected onto the ground). Along-track ground resolution at full-width-half-maximum will therefore be almost equally affected by

Table 3: Sensor design and performance characteristics.

Design and performance parameters	Baseline design and performance values	Notes
Nominal altitude	$788km$	For ground sampling distance (GSD)
GSD along-track at nadir	$25m$	$100m \times 100m$ at extreme pitch angle
GSD across-track at nadir	$50m$	$100m \times 100m$ at extreme pitch angle
Image area	$50km \times 50km$	Variable along-track
Modulation transfer function	>0.2 at Nyquist	Along- and across-track
Spectral range, VNIR	$400nm–1000nm$	Dichroic split at $\sim 940nm$
Spectral range, SWIR	$900nm–1700nm$	
Spectral resolution, VNIR	$<10nm$	
Spectral resolution, SWIR	$<12nm$	
Number of spectral bands recorded at zero pitch	120	At maximum spatial resolution
Number of spectral bands recorded at non-zero pitch	20	At maximum spatial resolution
Number of images per target-overpass	7	
Absolute response accuracy	5%	After vicarious calibration
Out-of-field stray light	$<1\%$	Of scene radiance
Out-of-band stray light	$<0.1\%$	Of band average radiance
Signal to noise ratio, VNIR	500 typical for range	See §3.1.7
Signal to noise ratio, SWIR	300 typical for range	See §3.1.7
Wavelength knowledge	$\pm0.5nm$	
Spatial registration	$<5m$	All wavelength
Spectral registration	$<1nm$	Full field
Number of image sets recorded per day	10	
Digitization	12 bits	Gain stages extend dynamic range
On-board data compression	Typical factor 2	Lossless
On-board mass memory	2 Gbytes	Includes 10% overhead for EDAC and housekeeping

slit width and motion smearing, and will be set approximately equal to the along-track ground sampling distance.

Motion compensation and pitch rotation   The scan rate of the line-field over the Earth surface will be controlled by adjusting the platform pitch. In general, the scan rate over the ground will be reduced to allow an increase in integration periods and a reduction in output data rates from the detectors. This will improve performance in terms of both signal-to-noise ratios (SNR) and the number of spectral bands that can be read out at full spatial resolution. The factor by which scan rate is reduced, compared with operation in simple nadir-pointing mode, is called the Motion Compensation Factor.

The science requirements demand several views of each selected area, recorded at different angles during a single overpass. This requires control of platform pitch typically over the total range $\pm 60°$ with respect to the nadir-pointing attitude. The typical pitch-motion for an image set can be considered to be the smooth motion required to stare continuously at the centre of the target image, with a superimposed oscillation that generates scan over the required image area. It is efficient to scan forwards and backwards over the image area in successive area scans. The platform attitude control requirements therefore depend on, and in practice will constrain, (i) the number of images recorded in each overpass, (ii) the along-track size of each image, and (iii) the motion compensation factor. The relationship between these factors and the attitude control is complex. It will be feasible to provide the required baseline performance parameters listed in Table 3 for the 'standard' operation mode and other required modes.

Detailed optical design   The instrument optics will be designed as indicated in Figure 6. Basic parameters of the current baseline design are given in Table 4. Note that the along-track spatial resolution ($25m$ at nadir) is determined at the entrance slit, which is only $0.015mm$ wide, while spatial resolution across-track ($50m$ at nadir) is determined by the detector element size, which is $0.03mm$. The optical performance given in Table 4 are computed from design, without allowances for manufacturing defects but, we would expect to achieve the requirements listed in Table 3.

All optical elements, including the mirrors, will be made of fused quartz. This provides high transmission through the spectral range, with no measurable effects of space radiation. The mirror surfaces will be given silver-based coatings, with dielectric layers to enhance reflectance in the deep-blue region. Single-layer anti-reflection coatings will be applied to the refracting interfaces to improve transmission in selected spectral regions.

Telescope and entrance slit   The telescope design is selected for compactness and ease of manufacture. It is an axially-symmetrical, two-mirror system with a concave primary and convex secondary mirror, with lens elements added to improve aberration correction over the required field. Both telescope mirrors are moderate aspherics: all other surfaces in the whole optical system are spherical or flat. A single, near-flat window at the front of the optical system will seal the system against contamination and will also support the secondary mirror.

The entrance slit will be formed in a metallic layer on the rear surface of the last element in the telescope system. This surface is tilted $10°$ with respect to the telescope axis and is sealed by a cemented lens element, which effectively forms the first element of the spectrometer optical system. An over-sized slit on the cemented surface of the first spectrometer element will increase the optical density of the combination to > 6.

Table 4: Baseline optical design parameters.

|	
Telescope field angle	
Across-track	3.64 ($50km$ on ground at $788km$, nadir)
Along-track	6.5 arc seconds ($25m$ on ground)
Telescope focal length	$473mm$
Telescope aperture diameter	$200mm$ (f/2.4)
Aperture obstruction diameter	$120mm$
Transmission	50% to 70% (excluding dichroic split)
Telescope blur along-track	$<0.007mm$, full spectrum, worst case
Entrance slit width, length	$0.015mm$, $30mm$
Spectrometer magnification	1.00
Image width across-track	$30mm$
Spectral spread $400nm$–$900nm$	$4.6mm$
Spectral spread $900nm$–$1700nm$	$2.4mm$
Spectral resolution (corresponding to $0.03mm$ detector row width)	
$400nm$	$1.1nm$
$900nm$	$8.5nm$
$1700nm$	$9.5nm$ ($10.6nm$ maximum at $1280nm$)
System blur acrosstrack	$<0.025nm$
Spectrometer blur, spectral	$8nm$ worst case
Spatial registration (frown)	$<5\%$ of across-track GSD
Spectral registration (smile)	$<3\%$ of spectral resolution
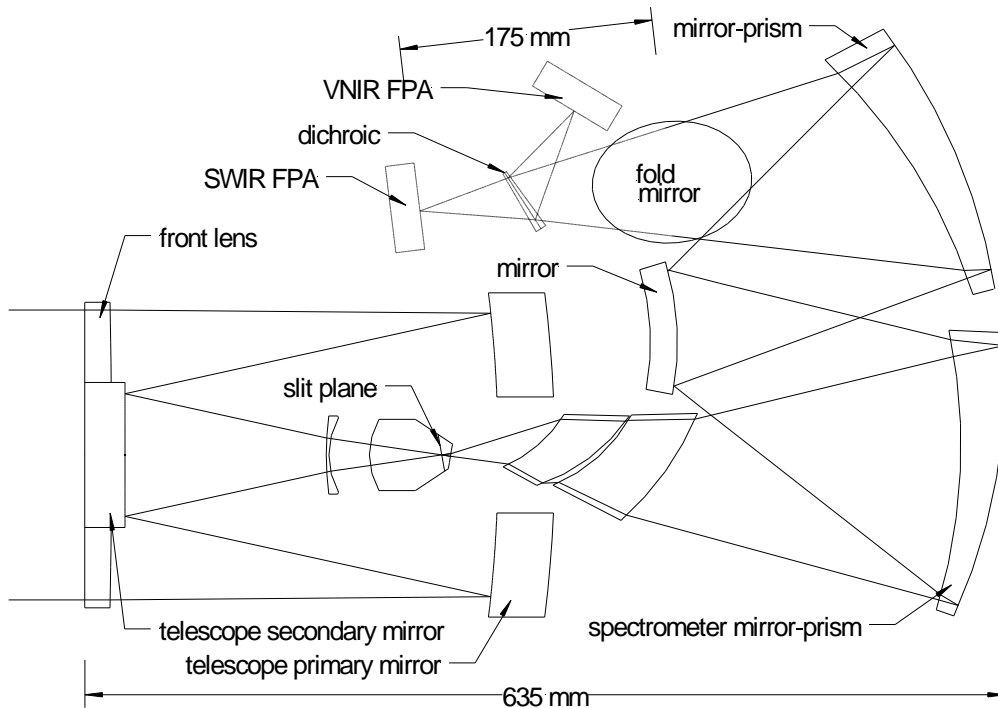
Figure 6: Optical design

Spectrometer   The spectrometer optical design is derived from the Offner relay form. It re-images the entrance slit, with the required spectral spread, onto the VNIR detector. A dichroic mirror in front of the detector splits the beam, reflecting part to the SWIR detector. Curved refracting wedges are added to the two large concave mirrors to provide most of the required dispersive power. Two meniscus lenses are introduced into the path between the entrance slit and the first spectrometer mirror. The path from the third curved mirror to the focal plane is kept free of lens elements to provide space for a fold mirror and a dichroic. The fold mirror is at $45°$ to the meridian plane of the telescope-spectrometer system: elements and light paths following the fold are therefore out of the meridian plane, but are indicated in Figure 6 by dashed lines. The fold is useful in placing the SWIR detector close to the cold face of the platform, where it can be cooled most efficiently.

A dichroic is inserted in the path between the fold and the SWIR detector, which reflects the VNIR wavelengths to the VNIR detector. The dichroic is a cemented assembly of two wedged plates, with the dichroic coatings on one of the cemented faces. It is used at a low angle of incidence to maximize efficiency around the 50% reflectance-transmission point, which is set at approximately $940nm$. Aberrations of the wedged elements on both paths are corrected within the preceding spectrometer optics.

Stray light control   Stray light in the telescope will be controlled by (i) tilt of the entrance slit plane, which will direct incident light (outside the slit itself) onto a black side surface; (ii) conical baffles in the space between the two mirrors, which will prevent light from reaching the slit without reflections at both mirrors, (iii) conventional blackening of most internal structure surfaces, and (iv) pupil imaging onto a stop (secondary mirror) in the spectrometer.

The external baffle will have only a minor impact in stray-light control — its major importance is in reducing variations in thermal radiant inputs to the telescope optics. The most significant residual generated in the telescope will be due to double reflections between some optical surfaces, optical surface scatter and scatter from baffles. This will generate out-of-field stray light, expected to be below 1% of the average scene radiance. Very little stray-light is expected to be generated in the spectrometer.

3.1.2   Detectors and detector operation

The detectors for the PHI instrument will be:

- A Cadmium Mercury Telluride (CMT) area-array detector currently under development at SOFRADIR for ESA (originally for the LSPIM programme, but now for similar hyperspectral missions).

- A frame-transfer CCD, thinned and back-illuminated for high quantum efficiency over the spectral range from $400nm$ to $>900nm$.

The CCD format needs to be matched to that of the SWIR detector, to permit spatial registration between the VNIR and SWIR spectral data without re-sampling. For this reason, the CCD will be a new development. However, it will use no new technology, and can be produced within the development period planned for PHI. Detector design and critical performance characteristics are listed in Table 5.

The SWIR detector is currently predicted to have a quantum efficiency averaging 0.7 between $900nm$ and cutoff. We have assumed a quantum efficiency of 0.6 for all radiometric calculations. The VNIR detector will have a spectral sensitivity typical of thinned, back-illuminated CCDs.

Table 5: Detector design and performance characteristics.

Design and performance parameters	SWIR detector	VNIR detector
Columns in image area	1000	1000
Rows in image area	256	256 (same in storage area)
Element size	$0.03mm \times 0.03mm$	$0.03mm \times 0.03mm$
Number of readout ports	4	2
Number of rows read	60 (after skipping)	60 (after binning)
Operating temperature	$<175K$	$<300K$
Spectral range	$900nm$–$1700nm$	$400nm$–$980nm$
Cutoff wavelength	$2000nm$	
Dark signal at EOL	<0.3pA per element	<0.01pA per element
Number of reads per cycle	2 (1 option)	1
Output rate per o/p port	2 MHz	2 MHz
Read noise	150 rms electrons	50 rms electrons
Element saturation charge	$375,000$ electrons	$1,200,000$ electrons
Signal transfer period/read	Integrate-while-read	$750\mu s$ frame transfer
Calibration on chip	Overscan and masked pixels read in each frame	

For short wavelengths in the VNIR band, signals from the CCD will generally be binned in rows-sets to provide spectral resolution intervals larger than those produced by single rows. The CCD output must be calibrated for 'smear' signals, which are collected during the frame transfer period. This requires readout from a group of non-illuminated detector rows. Both the VNIR and SWIR detectors can dump signals from unwanted spectral regions to reduce readout requirements, where this is desirable.

Detector drive control and detector saturation　Detectors will be operated in a basic cycle time of $15ms$ which, with a motion compensation factor of 2, will provide an along-track ground sampling distance of $50m$, corresponding to the across-track sampling at nadir determined by the detector pixel size.

Detector saturation levels are significant in limiting the scene radiation that can usefully be collected and, hence, tend to determine the SNR that can be achieved over moderately and very bright scenes. Provisionally, the SWIR detector will be read twice during each imaging cycle, and the signals read in frame-pairs will be binned by means of digital processing to provide the nominal along-track sampling distance. This will increase the nominal effective saturation charge per pixel-cycle to $675,000$ electrons, at the cost of increasing read noise per cycle by a factor of $\sqrt{2}$. Depending on detector developments, this strategy may not be needed since the device can, in any case, be designed for larger saturation levels at larger read noise (for example, $1,625,000$ electrons at 400 electrons read noise is quoted).

Under these baseline conditions, both detectors will saturate at a scene radiance corresponding to approximately 0.5 albedo over the equator. We propose to use the baseline for most scenes — in which areas of interest will generally give signals below saturation — allowing the system to saturate on bright cloud. There will be options, however, to operate the detectors at shorter integration periods for studies on relative bright scenes, and at longer integration intervals for possible studies on scenes at very low radiances. In general, when using the system at integration

times shorter than the baseline, the numbers of separate spectral bands read will be reduced (below 120 at baseline), to maintain a maximum readout rate of $2M$pixels/s per output port.

Detector thermal control The VNIR detector will be operated, without specific cooling, at a convenient temperature likely to be in the region of $270K$. The SWIR detector requires cooling to limit effects of dark signal and dark signal non-uniformity (DSNU) on SNR and absolute accuracy. The most significant problem is the control of temperature variations in DSNU, that will require moderate temperature stabilization between significant calibration cycles, depending on mean temperature. Provisionally, the detector will be operated at about $180K$, with variations held within $< 1K$ between full dark-level calibrations. This may be achieved by passive cooling only, but provision can be made for inclusion of a single-stage thermoelectric device, operating at a low nominal differential, used essentially for stabilization.

Detector radiation effects and shielding Approximately $6mm$ (minimum) thickness of aluminium-equivalent shielding will be provided for the detectors to limit the total radiation dose over 5 years to $< 5krads$. The received dose, dominated by trapped protons, will increase dark signal and DSNU, and introduce Random Telegraph Signal (RTS) in the CCDs. The dark signal effects, including short- and long-term temperature variations, will be largely corrected by the proposed calibration procedures. RTS cannot be calibrated: it is expected to be less significant than photon noise, but will be reviewed during Phase A — it may be desirable to run the CCD at a temperature below the current baseline. The protons will also reduce Charge Transfer Efficiency (CTE) in the CCDs. Relatively large signal levels will be generated by PHI, so that worst-case inefficiency (CTI) at EOL will be in the region of 0.00003 per transfer — typically 1.5% delayed charge for 500 transfers. This is expected to have only very minor impacts on spatial and spectral resolution and wavelength calibration.

3.1.3 Proximity (analogue) electronics

Analogue electronics will be located close to the detectors, provisionally in a single box, and connected by flexicircuits nominally $< 150mm$ long. One PCB will be used for each detector output line. The electronics will receive power and framestart signals, and output raw digital data, provisionally on six lines (one per detector output). They will provide conventional detector drive and signal processing functions, including (i) supply conditioning and generation of detector-drive waveforms, (ii) correlated double sampling, limiting and level shifting, and (iii) amplification of output and digitization at 12-bits. Box dimensions will be in the order of $200mm \times 150mm \times 75mm$ and mass in the region of $1kg$. Power dissipation in proximity electronics will be in the region of $15W$ while the instrument is imaging.

3.1.4 Instrument structure and thermal control strategy

The main instrument structures will be made in Carbon-Fibre Composites (CFC) and CFC-faced aluminium honeycomb, with inserts to provide interfaces to components mounts (*e.g.,* spectrometer mirrors) and the platform. Low thermal expansion in the structures, combined with low expansion in the optics (fused quartz) will ensure that the instrument stays in focus over large uncertainties in operating temperature. It will also, in general, make the system insensitive to spatial gradients of temperature and ease problems of mounting optics.

In general, stresses to refracting-only elements will not present significant problems, and simple mounting methods can be used. Special attention will be given to detailed design of mirror mounts to ensure that the elements are not stressed during mounting or system assembly. The present concepts make use of Invar sub-frames into which mirrors are mounted. Each frame is then mounted on the main structure via three ball-joint/flexures that provide adjustments on the required degrees of freedom prior to bonding. The telescope secondary mirror will be mounted on the front lens (as in the CHRIS instrument), via an Invar flexure frame.

The telescope system will be aligned by conventional methods for axially-symmetrical optics. Alignment of the spectrometer involves location of the centres of curvature of all optical surfaces at correct relative positions. This will be done (as for CHRIS) using a modified auto-collimator (with a focusing lens) mounted on a coordinate measuring machine. Critical adjustments for the detector and entrance slit include focus and rotations in the focal planes (the latter are required for spectral and spatial registration). The instrument will be mounted by an isostatic system, using flexures to the spacecraft payload panel.

The instrument will be thermally isolated from the platform using low-conduction feet and MLI wrapping. The proximity electronics will be separately mounted on the platform to avoid thermal disturbance to the optics. There will be a thermal break between the telescope and the spectrometer. The SWIR detector will also be thermally isolated from the spectrometer structure using rigid titanium blades. The main thermal disturbance to the telescope will be variations in radiant interchange with the external scene. This will be expected to alter temperatures within the telescope by upto a few degrees through the orbit; however, this will not produce significant changes of focus. The main disturbances to the spectrometer will be due to residual heat exchanges with the telescope, the detectors and the platform structure. The spectrometer temperature is expected to change by $< 0.2°C$ through the orbit, but is likely to change by a few degrees owing to through-life degradation in the platform thermal control surfaces.

The most significant concern for thermal stability of the optics is the effects on wavelength calibration. If uncompensated, the calibration will change by $1nm/°C$ change of temperature, owing to the refractive-index variation of the refracting elements. This will not be significant through the orbit, but could be significant through life. Wavelengths will be re-calibrated periodically through life, so that it is not necessary for users to make significant modifications to their data-processing algorithms. Provisionally, it is proposed to correct the systemmatic wavelength-shift by a minor adjustment to the design of the spectrometer structure (for example, by incorporating a length of aluminium in one of the two rear mirrors).

3.1.5 PHI calibration

Procedures for calibration of the instrument are summarized in Table 6. The most difficult problem in calibration of space-based radiometers in the solar spectral region is in measurements of absolute spectral response in-flight. A commonly-proposed solution is to deploy a sun-illuminated diffuser over the instrument aperture. However, this requires a large sub-system, including a critical movement, and does not provide high confidence levels since diffuser reflectances have been found to degrade after pre-flight calibration. Some on-board hardware schemes have included multiple diffusers. This approach (initiated by Sira for MERIS) gives some improvement in confidence, but does not provide an ideal independent check.

For PHI, we prefer to rely essentially on vicarious calibration for measurement of absolute response, and response non-uniformity across the field, as outlined in §3.6. These measurements will be supported by use of small, sun-illuminated diffusers on board. Diffuser measurements will

Table 6: PHI calibration summary

| Parameter calibrated	Method for generation of calibration data	Accuracy and data update frequency required
Electronic offsets	Overscan pixel signal	Sub-noise, 10 seconds
Full dark-field pattern	Dark images recorded in eclipse	Sub-noise, 7 days
Dark-field variation with detector temperature	Signals from masked pixels	Sub-noise, 10 seconds
Pre-flight full-field spectral response pattern	Ground calibration using radiance standards	$\pm 5\%$, pre-flight
Change in field-average spectral response after launch	Small, sun-illuminated diffusers (see below)	$\pm 1\%$, once per month initially
Absolute spectral response (corrections to pre-flight data)	Vicarious calibration	2% (or best affordable), within 6 months of launch and once per year
Change in spectral response pattern over the field (corrections to pre-flight calibration)	Averages of large data volumes collected over bland scenes	Sub-noise at pixel-to-pixel level, within 6 months of launch and once per year
Full wavelength calibration	Pre-flight calibration, using spectral lamps	$< \pm 0.5nm$, pre-flight
Corrections to full wavelength calibration after launch	Small, sun-illuminated diffusers with etalons (see below)	$< \pm 0.5nm$, after launch and initially once per month
Linearity and saturation	Ground calibration using radiance ratios	$< \pm 1\%$ at radiances down to 5% of saturation
In-flight linearity check	Ratio signals from LEDs in spectrometer	$< \pm 1\%$, 6 months
Stray light	Full BRDF data recorded on ground — laser sources at 3 (TBD) wavelengths	$\pm 10\%$, pre-flight
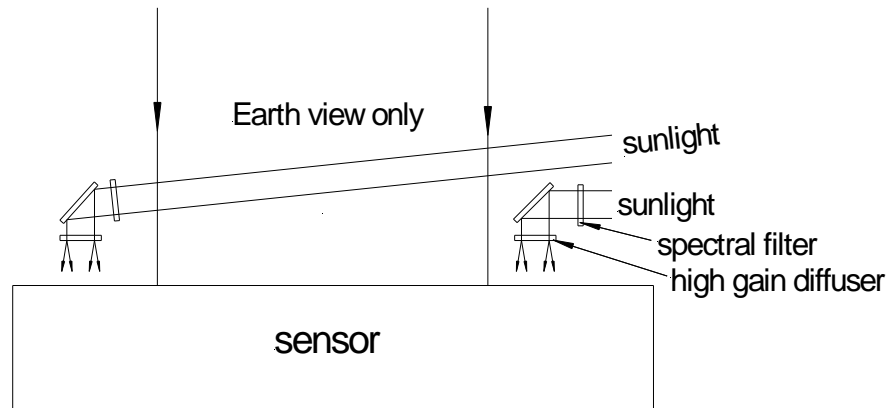
Figure 7: In-flight calibration of wavelength and stability of spectral response.

provide relatively frequent absolute measurements, at least once per month during the initial period after launch.

The proposed on-board diffuser method is illustrated schematically in Figure 7. At least two diffusers will used. They will be permanently fixed in position over the optical aperture, occupying a total of about 3% of the total aperture area. No mechanisms will be required. The diffusers will be sun-illuminated only as the platform exits from eclipse, while the remainder of the aperture receives no significant light from the scene. The diffusers will be baffled to receive no significant illumination while the platform is over sunlit Earth. Transmitting diffusers will be used, with a photometric gain of about 10, providing signals typically equivalent to a scene of about 0.1 albedo when illuminated by the Sun. The concept has been elaborated in a study funded by ESA (Calibration Requirements for Hyperspectral Applications) in which properties of transmitting diffusers were measured.

Spectral filters will be incorporated in at least one of the filter assemblies to provide spectral signatures for in-flight wavelength calibration. The baseline proposal is to use stable Faby-Perot etalons, that will provide spectral lines in both the VNIR and SWIR bands.

3.1.6 *Attitude control requirements for PHI on BIOSAT*

For each target area, a set of images (7 in 'standard' mode) will be recorded at different along-track angles during a single overpass. This requires special control of platform pitch and roll through the image-set overpass. Typical requirements on platform pitch and pitch rate are illustrated in Figure 8, which shows pitch and roll rates, with respect to a celestial reference frame. It is assumed for this calculation that pitch rates are nominally frozen during image recording periods, and varied at constant pitch-acceleration rates between image takes to minimize torque requirements. The pitch rates during imaging provide a standard-mode motion compensation factor of 2.

Figure 8 shows the period from initiation of the first image-take to the end of the last image-take. Before this, the platform will, of course, be required to pitch backwards to view forwards, and then adjust pitch rate for the first image. Following the last image, it will be pitched forwards, and may then return to a normal pitch attitude before the next imaging manoeuver. In these example plots, the nominal view angles with respect to the local vertical used in this example are $\pm62°$, $\pm41°$, $\pm21°$ and nadir. Except for vicarious calibration, calibration data will be acquired in a nominal nadir-pointing attitude over dark Earth, with TBD yaw adjustments to accept sunlight in the required directions.
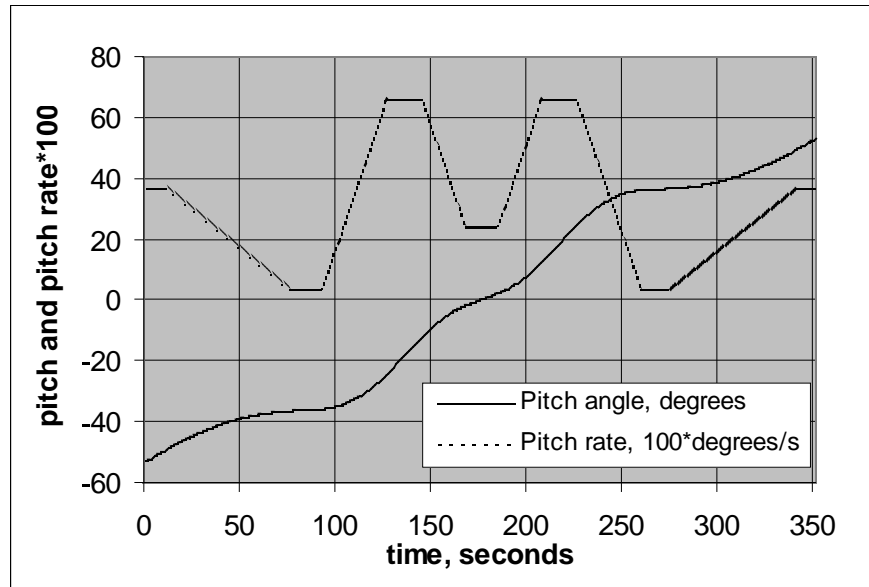
Figure 8: Pitch and pitch rate plots for a set of 7 images.

In general, roll adjustments are also required during the image-recording manoeuver, to keep the target in the centre of the instrument field, but these requirements are much less severe than for pitch.

The maximum computed angular acceleration on the pitch axis, in the assumed scenario, is $0.018°s^{-2}$. This will be increased by allowances for settling *etc.*, and will preferably be exceeded to provide some general performance margin. The maximum computed pitch rate (which depends on the selected motion-compensation factor, and will preferably also be exceeded by platform capabilities) is $0.66°s^{-1}$. Standard mode presents the most stringent requirements on attitude control. 'Fine sampling' mode can be defined to work within the attitude-control capabilities required to record 7 images in standard mode. For example, a sinusoidal pitch-perturbati-2on scanning a $10km$ along-track strip at nadir can be performed at $0.22Hz$ (giving $0.44Hz$ image rate) within the $0.018°s^{-2}$ angular acceleration limit, to provide images at angle-intervals of about $1.1°$ at nadir. The aim is to provide dense BRDF sampling only for a narrow strip of resolved points on the ground: a small along-track scan relaxes the requirements on relative pointing accuracy and provides spatial over-sampling along-track to allow identification and selection of superimposed pixels.

3.1.7 *Instrument performance*

The instrument performance is expected to meet or exceed the requirements listed in Table 3. SNRs have been computed for operation in the standard mode, for scene albedos of 0.05 and 0.3 at latitude $45°$ during the vernal equinox. Results are plotted in Figure 9. The model includes (i) photon noise on all signal, (ii) effects of CCD smear, detector read, electronics and digitization noise, (iv) DSNU at EOL, including uncalibrated temperature variations and an allowance for RTS. Sharp variations in computed SNR in the region $400nm$–$800nm$ are associated with variations in binning of detector-row signals to achieve the largest feasible fractions of $10nm$ spectral resolution.
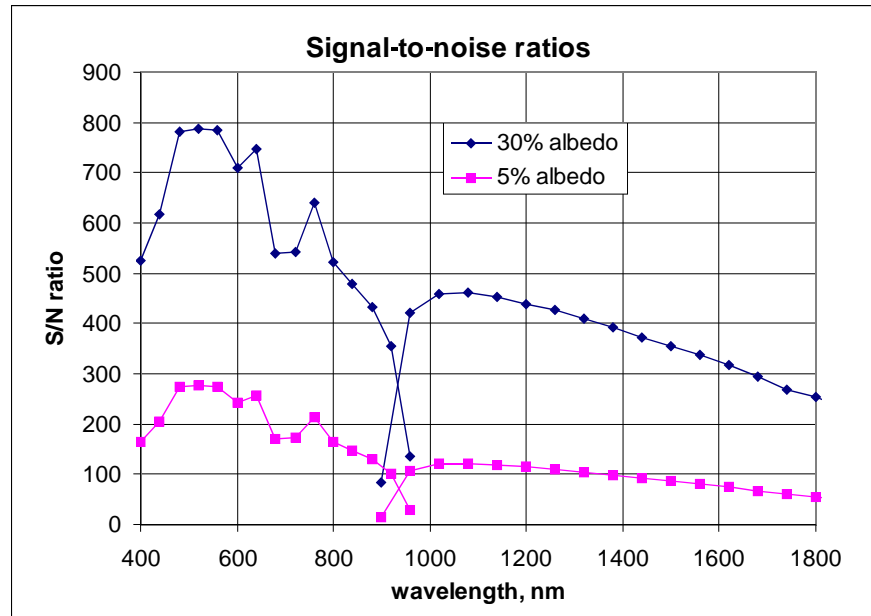
Figure 9: Computed signal to noise ratios.

3.1.8 *Instrument heritage and risk areas*

The design of the sensor has immediate heritage in the Sira CHRIS instrument, recently launched on the ESA PROBA platform. Aspects demonstrated by CHRIS include:

- Two-mirror catadioptric telescope and spectrometer with curved prisms,

- Telescope, spectrometer and CCD thermal control,

- Stray-light control,

- Detector readout flexibility,

- Analogue electronics essentially as proposed for PHI,

- Offset and dark-level calibration methods, including temperature variations,

- Sun-illuminated device over part of the aperture for in-flight response calibration, and

- Level 1a data processing.

Useful lessons have also been learned from CHRIS. For example, the CHRIS calibration device used a single lens — this produces fine spatial structure in the focal plane due to otherwise undetectable ripple in the surfaces of the optics — small diffusers will be preferred for PHI. The CHRIS concept will be elaborated principally in:

- Inclusion of a SWIR detection system,

- More stable structures, and

- Inclusion of wavelength-calibration filters (and diffusers replacing lens).

The proposed instrument development is generally considered low-risk. The most significant concerns relate to development of the detectors. The VNIR detector is a new development, although it will require no new technology, and the required performance parameters have been demonstrated in other devices (in feasible combinations). The SWIR detector is approaching the end of its initial development, but will (we assume) not previously have been flown on a space mission. It will be necessary to space-qualify both detectors, with respect to resistance to mechanical and thermal stresses and space radiation. The SWIR detector may be produced in a special batch with a cut-off wavelength reduced to about $1800nm$ (TBC). However, it is expected that both detectors can be produced within an acceptable time-frame.

Concerns to be addressed in Phase A will include optimization of the thermal control for the SWIR detector. However, initial analysis indicates that the required performance can be achieved by the baseline approach and there is substantial margin against serious technical risk in the present proposal:

- Performance predictions are based on a cut-off at $2500nm$, which can be reduced to about $1800nm$,

- A thermoelectric temperature control can be added, and

- The proposed calibration scheme will, in principle, correct for temperature variations in DSNU.

3.2 BIOSAT Platform

The BIOSAT scientific objectives require images of a target site to be taken from seven angles in multiple spectral channels in both the VNIR and SWIR spectral regions. The main technical drivers imposed on the platform design by the mission science requirements are:

- **Agility** to allow multiple views of a target site in a single pass, image motion compensation, off-track pointing and platform steering for data down-linking.

- **Thermal control** to maintain the SWIR detector at a temperature which permits the required radiometric resolution, and ensures that temperature stability is kept throughout the duration of the mission.

- **Data handling** to store and down-link the large amount of data generated by the multiple view measurements (typically 10Gbits per scene).

Figure 10 shows two views of the proposed configuration for BIOSAT with the PHI payload accommodated partially within the spacecraft structure. The left view shows the radiator panel and Earth baffle used for the passive cooling of the SWIR detector and the star-tracker orientation. The right view, with the sun-side panel cut away, shows the location of the PHI instrument. The centre view shows the internal configuration.

The multiple view requirements of this mission will involve substantial, controlled platform steering. The agility required for the controlled platform pitch-and-roll drives the platform design towards a compact spacecraft, with no deployable elements, to provide maximum stability.

The PHI payload will require a cooling system to cool the SWIR detector to $180K$ and to provide temperature stability better than $1K$. The platform design is optimized to provide passive cooling to the payload SWIR detector by means of a large-area instrument radiator, a radiator
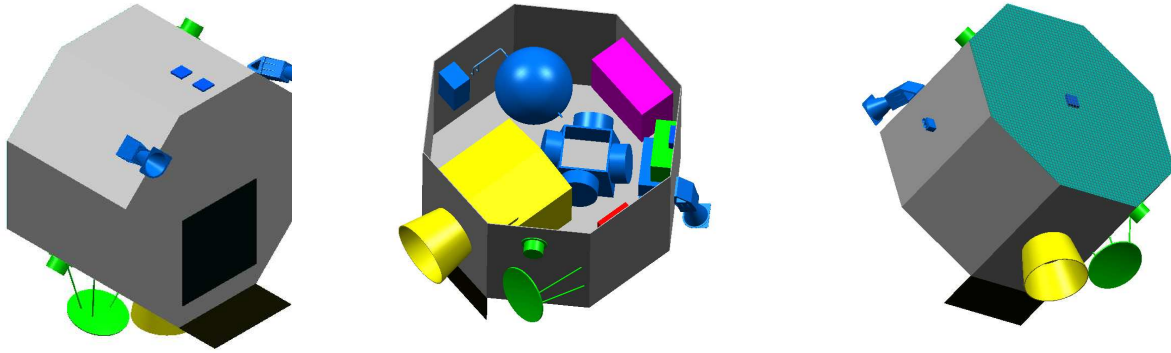
Figure 10: Preliminary concept for the BIOSAT configuration.

baffle and a configuration that locates high power units away from the instrument detectors. This approach has been assessed in earlier studies funded by the BNSC (a full list of previous study work carried out by the team is provided in the Annex).

The PHI instrument generates a large amount of science data for each site: 10Gbits of data are generated as standard. To transmit all the science data collected, an X-band data down-link is required. The spacecraft and mission architecture is designed to support a 50Mbit/sec data link that minimizes the power mass and cost requirements.

A preliminary spacecraft concept has been derived which is compatible with the science mission and maximizes the use of existing designs and hardware. The mechanical architecture is based on an octagonal main structure, manufactured from solid CFRP. This has advantages of minimum thermal distortions, structure- and parts-count and, hence, low risk and high confidence in mass. The thick-skinned, CFRP monocoque technology has recently been qualified under BNSC funding. The BIOSAT avionics is based on the Leostar multi-mission avionics developed for high accuracy LEO missions for Earth observation and science. It is organized around a centralized computer which interfaces with off-the-shelf units for attitude measurement and control.

3.2.1 Guidance, Navigation and Control System

The AOCS concept is based on a gyro-stellar attitude determination and control system. This uses a combination of continuous, three-axis gyro measurements and autonomous star-sensor inertial-attitude measurements. The gyro data and stellar data are merged through a Kalman filter to provide pointing-stability and pointing-knowledge information. A set of reaction wheels provides the actuation control. A propagated on-board ephemeris provides the means to relate the inertial attitude to the Earth-referenced target attitudes. The ephemeris is generated from accurate GPS measurements and on-board algorithms.

To perform the observations in the operational phase, steering laws will be generated from the pointing target data and applied to the spacecraft to provide the correct pointing-attitude during the observations. The main manoeuvre axis is the pitch axis that is required to move around approximately $120°$ during each imaging overpass. Within this period, steering is performed by modulating the coarse pitch movement, with additional control for each of the separate scans. The wheel configuration will be sized, accordingly, for the pitch-torque demands.

AOCS equipment   The AOCS design is based on the Leostar architecture, with the equipment listed below optimized to meet the system requirements for the minimum cost:

- Autonomous Star Tracker (AST) — two star-trackers operating in cold redundancy provide three-axis inertial attitude data; the AST bore-sight is oriented to avoid sun blinding and earth intrusion;

- Gyro — provides continuous three-axis attitude data; a non-mechanical gyroscope (baseline: ring laser gyro) is required to enable continuous use in all three axes;

- Sun Acquisition Sensors (SAS) — provide almost spherical coverage, sun-referenced attitude data;

- Reaction wheels — provide three-axis control torques;

- Magnetorquers — provide wheel off-loading capability; and

- GPS receivers — provide autonomous, high precision, on-board orbit determination.

In addition, a processor will be required to perform on-board attitude determination and ephemeris generation plus the AOCS processing.

The BIOSAT spacecraft needs an orbit control capacity to correct for injection errors, perform periodic orbit maintenance, collision-avoidance manoeuvres and end-of-life de-orbit. The required delta-v budget has been calculated and is shown in §3.2.6. The preferred propulsion subsystem for the BIOSAT spacecraft is hydrazine. Hydrazine sub-systems have been used extensively on previous space missions, and continue to be used on many low Earth orbit missions. Therefore there is extensive heritage and a wide range of COTS hardware available with flight heritage. A single hydrazine thruster (plus one in cold redundancy) performs the velocity impulse, the spacecraft remaining three-axis stabilized by means of the reaction wheels.

3.2.2 Thermal Control System

In the selected orbit, one wall of the satellite will never receive direct solar illumination and the opposite wall will receive constant solar illumination, except when in eclipse. Part of the cold wall will be used as an instrument radiator to dissipate heat from the SWIR detector. This wall will, however, receive earth-shine and albedo fluxes and may need to be shielded to provide the required temperature stability through roll manoeuvres.

The thermal subsystem will be made up of standard thermal equipment, such as multi-layer insulation (MLI), optical surface radiators (OSR), thermostats and thermistors, heaters and thermal straps. Analysis has been carried out to verify the design concept with special consideration of cooling the SWIR detector. The general thermal structure uses OSR faces to dissipate the heat from the units inside the structure, with the cold-facing side used for the detector radiator only. All units inside the spacecraft will be de-coupled radiatively from all other internal components except for the panels to which they are attached. Heat pipes are embedded in the instrument radiator panel to utilize fully the radiator area owing to a single-point heat-source from the detector. Bonding the SWIR detector directly to the radiator, a detector temperature of $180K$ is achieved, with a $0.7K$ thermal stability. Planet fluxes of up to $10W$ are absorbed by the detector radiator, which could be reduced by increasing the size of the baffle if further cooling is required, but this would impact on the mass and size of the spacecraft. To improve the stability of the detector further, a thermoelectric Peltier cooler could be used.

3.2.3   Data Handling and Communications

The PHI payload generates 10Gbits of data per image set. The standard operational scenario is for one image set to be taken in each orbit where BIOSAT has access to the appropriate test sites. If Svalbard is used as the system ground station, contact is made in every orbit. To down-link one image set to Svalbard in the shortest pass, a data rate of 44Mbit/sec is required (including formatting and coding overhead). In some cases two images may be taken in a single orbit, therefore the mass memory unit is sized to store two sets of images at end-of-life. The mass memory selected at beginning-of-life is 32Gbits.

The science data will be transferred directly from the instrument into the solid-state mass memory. Data processing is then required to split the science data-packets into fragments which are compatible in size with the data-unit zone within the down-link data frames. The data down-link converts the formatted science data into a modulated RF signal and transmits it to ground. The preferred option for the down-link system is to use a fixed antenna with a moderate field-of-view and use the agility of the spacecraft to steer the beam onto the ground station antenna.

The TM & TC interface with the ground segment operates in S-band through two omni-directional antennas and a redundant S-band transponder. Both the TC processing/authentication and the TM packetization are compliant with the CCSDS standard.

3.2.4   Electrical/Power System

The Leostar generic avionics provides an electrical/power design which is compatible with the BIOSAT mission. The design provides a battery-regulated bus of nominally $28V$. The solar-array configuration is body mounted. The solar cells are mounted on the spacecraft wall that receives constant solar illumination when not in eclipse. A Lithium-Ion battery is selected and a battery-regulated bus will be used for simplicity, efficiency, and compatibility with the Leostar avionics. The added complexity of a fully-regulated bus is not necessary for the BIOSAT mission as all the chosen equipments have a wide operating voltage range.

3.2.5   Spacecraft functional architecture

The spacecraft functional architecture is shown in Figure 11 and a summary of the sub-systems and equipments is given in Table 7.

3.2.6   Spacecraft budgets

The BIOSAT spacecraft budgets are shown in Tables 8–10. With the exception of the payload, the essential functions are all redundant or sized with margin to provide high spacecraft reliability. The margin has been applied to each subsystem in accordance with the ESA standard requirements of: (i) completely new developments 20%; (ii) new developments derived from existing hardware 15%; (iii) existing units requiring minor/medium modification 10%; (iv) existing units 5%.

The total Delta-V budget for the five-year BIOSAT mission is shown in Table 10. The launch vehicle dispersion shows the range of Delta-V required to correct the injection error for the best-case launcher (DNEPR) and the worst-case launcher (PSLV).

Table 7: BIOSAT subsystem and equipments

| Subsystem	Unit	System description/heritage
PAYLOAD	Instrument Ins. Electronics	The payload instrument and electronics will be a custom design based on the Sira CHRIS instrument now flying on PROBA
GNC	Coarse Sun Sensor GPS Sensors & Receiver Magnetometer Star Trackers Intertial Ref. Units MagnetoTorquers	The GNC system is based on the standard architecture used on LEOSTAR platforms. The components selected are all space-qualified and have flight heritage
OBC	ERC32 MMU (32Gb)	The on-board computer for BIOSAT will be based on the systems for GOCE and ADM. The mass memory used has been developed for the Rocsat2 programme
Power	Solar Cells Battery 600 Whr LiIo	Body mounted solar array with triple junction GaAs cells. Redundant battery commercially available from SAFT or AEA
TTC	S-Band Antennas S-Band Transceiver X-Band Modulator X-Band Amplifier X-Band Antenna	S-band COTS equipment which supports CCSDS protocol X-Band data down-link with a data rate of 50Mbits/sec will be used for the instrument data
Propulsion	Latch Valve Thruster Pipework & Misc Tank Propellant	The BIOSAT propulsion is provided by a simple, modular hydrazine system with redundant thrusters
Mechanical	Structure S/C Thermal Harness Instrument Radiator	BIOSAT will use the filament-wound satellite-structure initially developed for the AMM study and recently qualified at Astrium. The thermal system is based on passive control using thermal isolation and a dedicated radiator to cool the SWIR detector
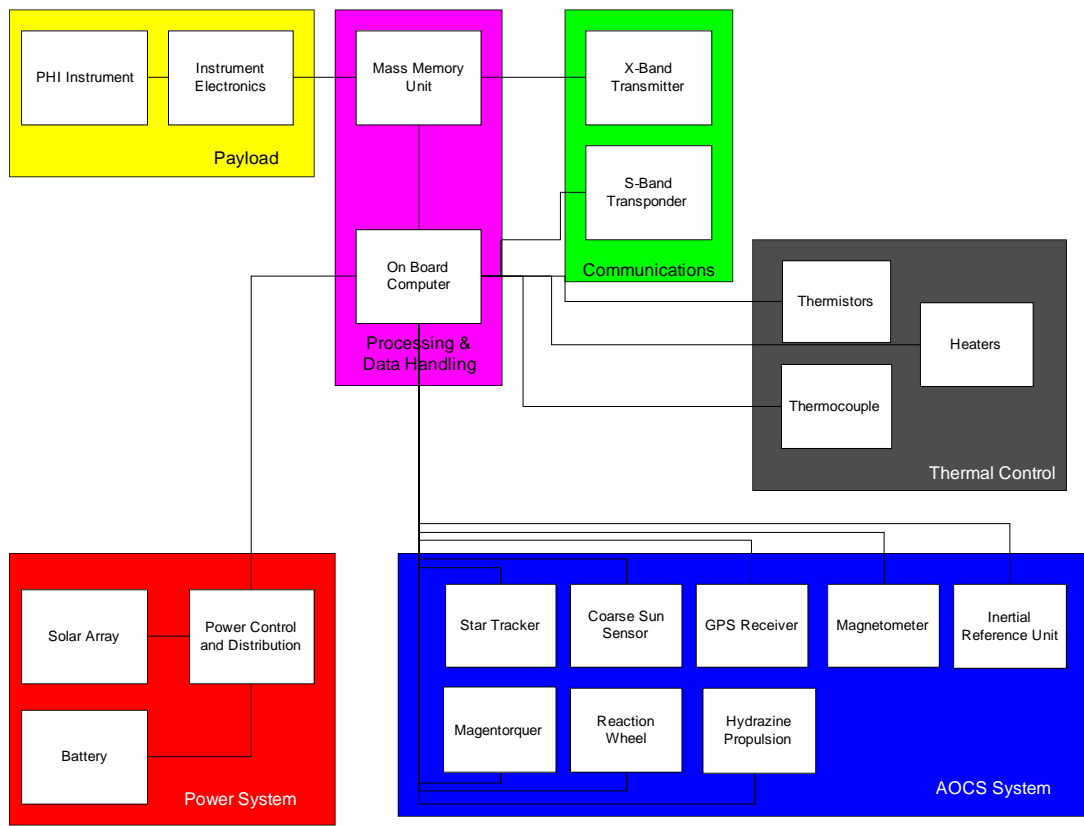
Figure 11: BIOSAT spacecraft functional architecture

Table 8: Mass budget

Subsystem	Mass (kg)	Margin	Mass incl. Margin
Payload	55	20%	66
GNC	50.5	5%	53
Data Handling	23	10%	25.3
Power Provision	11.5	10%	12.7
Comms Equipment	5.3	10%	5.8
Propulsion System	5.6	5%	5.9
Propellant	14.8	5%	15.5
Structure	23	20%	27.6
Thermal Control	5	15%	5.8
Harness	5	10%	5.5
Total	**198.7**		**223.1**

Table 9: Power budget

Sub-system	Peak Power (W)	Duty Cycle	Mean Power (W)
Payload	60	0.05	3
GNC	42.8	1	42.8
Data Handling	42	1	42
Power Provision	1	1	1
Comms Equipment	38	0.1	3.8
Propulsion System	-	-	-
Propellant	-	-	-
Structure	-	-	-
Thermal Control	3	1	3
Harness	3	1	3
Total	**189.8**		**98.6**

Table 10: Delta-V budget

Launch Vehicle Dispersion Error	5.6–31.8
Drag Compensation	1.5
Inclination Correction	29.4
Collision Avoidance	10
De-orbiting	76.8
Total	123.3–149.5m/s

Table 11: BIOSAT launch options.

Launchers	Mass @ S/S LEO 800km	Height accuracy (km)	Inclination accuracy (°)	Max Cost (M$)
LLV1 (Athena1)	>240	5	0.06	16
Cosmos	>800 main	40	0.08	12
Rockot	>800	16	0.05	13
PSLV	>1000	35	0.2	20
DNEPR	>250	4	0.04	12

Figure 12: BIOSAT accommodation in the Athena 1 launch fairing (left) and the DNEPR launch fairing (right).

3.3 Launch options

BIOSAT will be injected into a circular $788km$ sun-synchronous orbit with an inclination of $98.6°$. This orbit will have a 25-day repeat cycle and a worst case revisit time of 5 days at the using $\pm30°$ off-track pointing. The orbit height has been selected to allow enough time for the multi-angle observations of a science site to be made in a single pass, and the equator crossing time of $09:30$ has been selected to provide optimum viewing conditions. The launch options under consideration for BIOSAT are shown in Table 11. Secondary launches have not been considered at this stage because of the precise orbit characteristics required for the BIOSAT mission. With some of the larger launch vehicles listed it may be possible to consider accommodating a secondary payload to reduce the overall launch costs. The launch selection also depends upon the mission schedule if the BIOSAT mission is launched after 2007 converted ICBM launchers may not be available. The two options identified for a launch after 2007 are Athena1 and PSLV.

3.4 Ground segment and data acquisition

The BIOSAT ground segment, shown in Figure 13, consists of the following main elements:

- Command and Data Acquisition;

- Mission and Satellite Control; and

- Processing and Archiving.

The BIOSAT ground segment is based on a single ground station (Svalbard) for down-link and TT&C with external TT&C stations available for LEOP and backup. The command and data
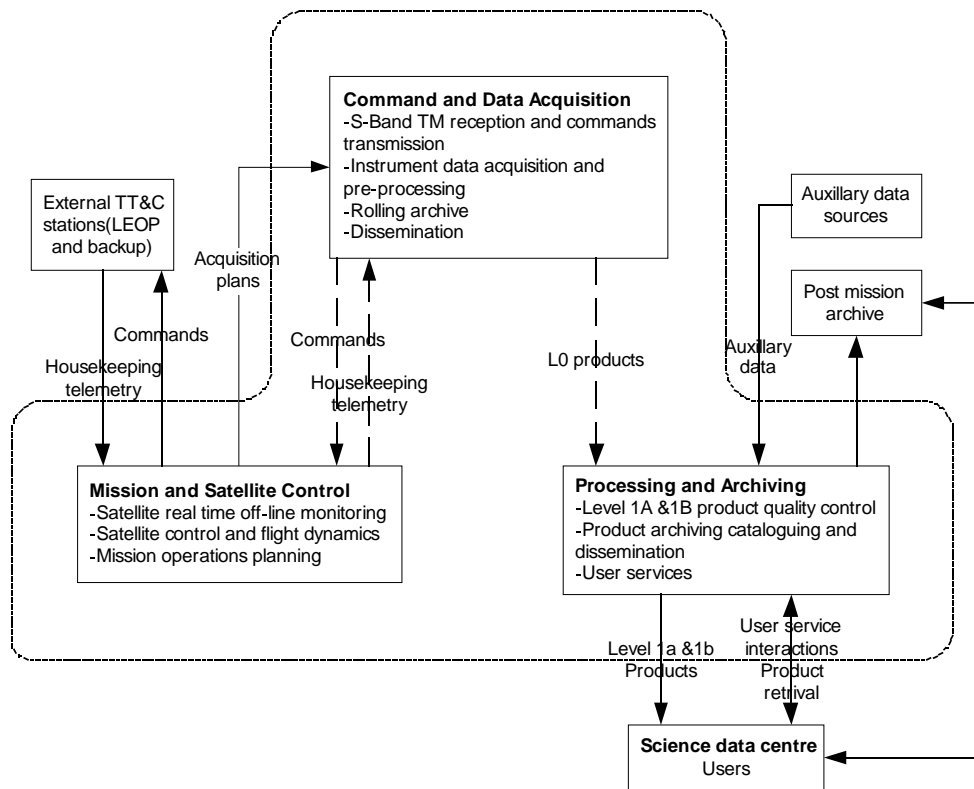
Figure 13: BIOSAT ground segment.

acquisition functions will be carried out at Svalbard (the baseline option is to lease time from the existing antenna). Because of the high latitude of the ground station, it is possible to receive the data acquired for a full image set in same orbit as the data are acquired. The data link is sized to receive a full image set in the minimum pass with an $11.3m$ antenna.

The mission and satellite control functions will be carried out at a remote site (ESOC) from which BIOSAT is operated and controlled via ground communication links to the command and data acquisition facility. The mission and satellite control facility will be responsible for operations of the spacecraft. It would also be responsible for the overall management of the space and ground segment during all phases of the mission. Routine TT&C contacts are anticipated in 6 orbits per day.

The processing and archiving facilities for the central processing functions to level 1b will be located at ESRIN. Complementary national facilities (*e.g.,* PAFs) could also be used. The science data centre (under the responsibility of the scientific community) will receive Level 1 processed data as input and generate value added products.

3.5   Data processing and dissemination

An indication of the approach to data exploitation and the maturity of necessary algorithms

3.6   Validation programme

Experience tells us that the transmissions of the optics may change by several percent from their pre-launch, calibrated values. Most effects are expected to be smooth, but not uniform, over the

spectrum. It is also possible that there may be some detector-to-detector changes, caused by debris being deposited on the entrance slit or detectors during launch. Radiometric calibration of sensor data must therefore include measurements made in-flight — these will require limited use of on-board hardware, but will critically include vicarous calibration exercises performed soon after launch and at TBD intervals thereafter. This will involve (i) capturing a multi-angle image set over a suitable calibration site and (ii) comparing the radiances against values predicted by radiative-transfer models. These models need to know the surface reflectance properties and certain atmospheric parameters.

Vicarious calibration of an instrument such as NOAA/AVHRR or Landsat-TM is made easier by the very limited number of detectors involved. With the BIOSAT/PHI, each across-track pixel has its own set of detectors and it is not feasible to generate, on the ground, the surface reflectance measurements that would be needed to calibrate every detector element. The most practical approach is to use detailed ground-based measurements to validate only a small area of the total field and to use data averaged over an image area selected for spatial uniformity to measure pre-flight to in-flight changes in pixel-to-pixel response non-uniformity.

The principal site to be used for radiance validation is the well-studied, high-altitude salt lake in Railroad Valley, Nevada, in the USA. This site is level, homogeneous and bright (albedo ~ 0.5) across all wavelengths. Its elevation is over $1000m$ so the aerosol loading in the atmosphere is low. It also enjoys clear skies for most of the year. This combination of factors maximizes the proportion of the top-of-atmosphere (TOA) radiance that is contributed by measurable surface reflectance and minimizes that due to uncertain atmospheric scattering. The uniformity of the site means that environmental radiance (*i.e.,* light reflected from the surface outside the IFOV, but being scattered by the atmosphere into the IFOV) is easily modelled. The near-Lambertian nature of the surface simplifies the coupling of the surface reflectance with atmospheric radiative-transfer models.

Measurements at the surface will consist of: (i) surface bidirectional reflectance factors (*i.e.,* directional radiance reflected from the surface relative to the reflectance from a standard panel) across all wavelengths; (ii) measurements of atmospheric transmission with a sun-photometer to estimate water vapour and aerosol loading, and measurements of the solar aureole to estimate the aerosol phase function; and (iii) spectral measurements of irradiance at the surface. The irradiance measurements will be used to constrain further the radiative-transfer (RT) model which is fed aerosol parameters from the sun-photometer measurements and surface reflectance values.

For the measurements at the satellite, two possible configurations of the sensor can be used. In the first, a full set of multi-angle images is required, as this gives seven radiance values instead of just the one at nadir. This will help to check the consistency of the aerosol data and the RT code used in the effort. This is the favoured method for checking TOA radiance values. In the second, the satellite will be yaw-steered through $90°$ so that the image of the entrance slit lies in the along-track direction. The data generated then consists of a long series of overlapping samples from a single profile, and each pixel along that ground profile is imaged by each set of detectors in turn. So, if the sub-satellite track is conceived as being formed of a long series of $50m$ pixels, the first 'line' of the 'image' captured in this mode consists of the spectra for pixels 1–1024, the second 'line' consists of the spectra for pixels 2–1025, and so on. This gives a very strong check on the relative gain of detectors, as a large number of samples is captured each of the detectors.

BIOSphere-ATmosphere interaction mission/Pointable Hyperspectral Imager (BIOSAT/PHI)

Table 12: Mission elements — implementation and funding source assumptions

Mission Element		Implementation	Assumed funding source
Science preparation	Scientific definition studies	Science team	ESA EEOM AO
	Campaigns	Science team	ESA EEOM AO
System engineering and assembly integration and test		Mission prime	ESA EEOM AO
Space segment	Instruments	PHI	ESA EEOM AO
	Platform	Leostar avionics with filament-wound structure	ESA EEOM AO
	Launcher	DNEPR (baseline)	ESA EEOM AO
Ground segment facilities	Command & acquisition stations	Svarlbard	ESA EEOM AO
	Operations centre	ESOC (baseline)	ESA EEOM AO
	Processing and archiving	ESRIN	ESA EEOM AO
Mission control and data exploitation	Mission control	ESOC (baseline)	ESA EEOM AO
	Data utilisation	Science team	National

4 Mission Elements and Associated Costs

4.1 Mission Costs

Mission elements and activities, and the funding source assumptions, are listed in Table 12, and cost estimates are presented in Table 13. (These two tables correspond to Tables 3 and 4 as required in the ESA Call for Proposals for EEOM.)

4.2 Development Plan, Schedule and Funding Profile

A space segment development schedule is presented in Figure 14, and a funding profile is presented in Figure 15.

Phase A of the space segment development will aim, critically, to optimize the expected science return within the accepted overall funding profile. It will include:

- Studies on science requirements to support space segment optimization,

- Preliminary instrument design and performance analysis, including specification of long-lead items (detectors),

- Preliminary platform design and launch plan, and

- Detailed planning for the subsequent development phases, launch and mission operations.

Phase B will provide preliminary detailed designs for the instrument and platform. Included within the time-scale of Phase B, detector developments will be started, and selected optics/mount assemblies will be breadboarded and tested.

Phase C/D will include the conventional detailed design, manufacture, integration and test exercises. Within the time-frame of Phase C/D, detection system breadboards will be built and tested, using the first available representative detectors.

Table 13: Mission cost Estimates

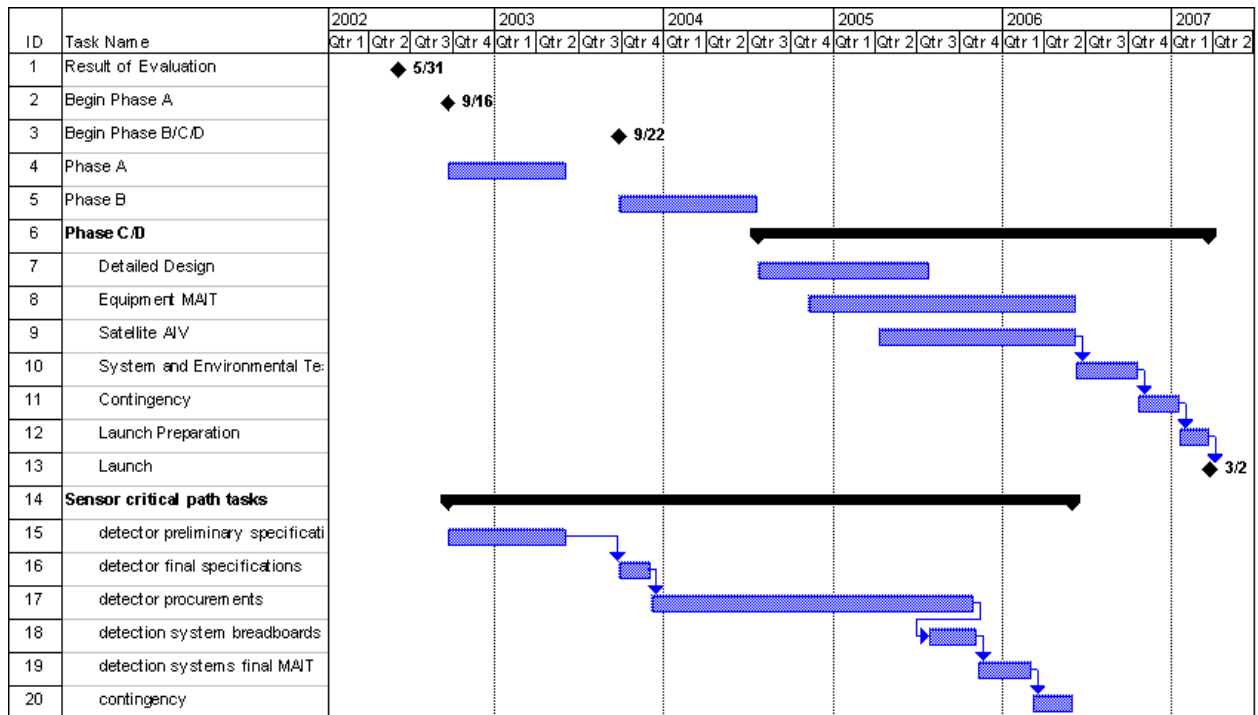| Mission Element		Cost Estimates	
		ESA	Other
Science	Science definition studies	1 Meuro	
preparation	Campaigns	0.5 Meuro	
System engineering and assembly integration and test		9.67 Meuro	
	Instruments	19.9 Meuro	
Space segment	Platform	26.78 Meuro	
	Launcher	12 Meuro	
	Command & acquisition stations	2.19 Meuro	
Ground segment facilities	Operations centre	4 Meuro	
	Processing and archiving	5 Meuro	
Mission control and	Mission control	2 Meuro	
Data exploitation	Data utilisation		2 Meuro
Totals			

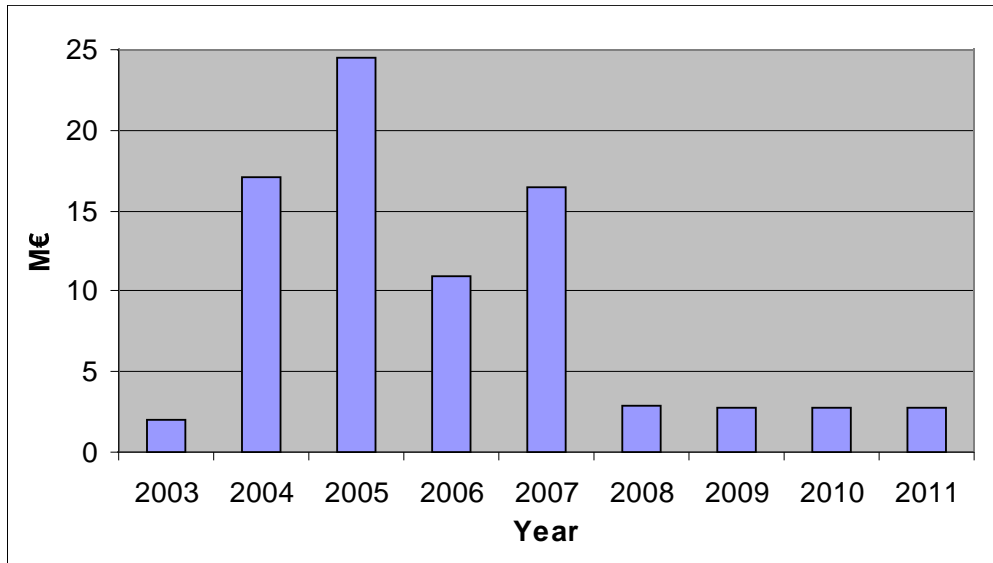Figure 14: Space-segment development schedule

Figure 15: Mission funding profile (ESA costs).

4.3 Basis for cost estimates and schedule planning

The basis for the cost estimates, and significant schedule drivers, are discussed below for the most significant items.

4.3.1 Science preparation

Workshops to discus science requirements?

Preliminary development of data processing algorithms (higher than 1a)?

Support to the engineering team on cost-performance trades (e.g. numbers of images against sizes of images, thoughts on resolution etc.)

4.3.2 System engineering and AIT

Costs for the system engineering and AIT are based on running an industrial prime project team, the facilities required for integration at the prime contractor and the test facilities required at ES-TEC. Costs for logistics and providing support to the launch campaign are also included.

4.3.3 Space segment — instrument

Cost estimates for the PHI instrument development are based on a proto-flight model philosophy, supported by specific breadboarding and test activities. Breadboards will include: (a) selected optical elements and mounting structures, tested for stability and freedom from stress on optics, (b) FPAs using representative detectors and analogue electronics, tested for performance over expected temperature ranges, (c) an in-flight wavelength/response calibration sub-systsem.

Delta developments and qualification testing will be required for the two detector types. A period of 24 months is allowed for delivery of flight models, after detailed detector specification (which must be completed early in Phase B).

Costs estimates for the instrument development, manufacture and test are based on similarity with other space instruments, including CHRIS (on the PROBA platform) and the Mid-Wave IR

Telescope (on the STRV2 platform), with weighting for complexity and QA requirements appropriate for the BIOSAT mission.

4.3.4 Space segment — platform and launch

The platform cost is based on a proto-flight model philosophy using current prices for the equipment selected and an estimation of the sub-system engineering effort required. The AOCS equipment and engineering effort needed to meet the BIOSAT agility requirements is the major component of the platform cost.

The cost estimate for the launcher is based on the use of a DNEPR ICBM launch, if the BIOSAT mission is launched after 2007 converted ICBM launchers may not be available. Athena 1 and PSLV have been identified as alternatives but will increase the overall mission cost.

4.3.5 Ground segment facilities, mission control and data exploitation

The ground segment facilities costs are based on the use of Svalbard for command and data acquisition and operations centre at ESTEC and a processing and archiving facility provided by ESRIN. The mission control costs are based on lights out operation with a single operator commanding and monitoring the spacecraft on a day shift Monday to Friday.

Explain basis for the data utilisation cost estimates

5 Implementation

5.1 Cooperation Arrangements

This proposal has been prepared with assistance from Sira Electro-optics Ltd and Astrium Ltd, who have collaborated on several space system developments, including parts of the CHRIS/PROBA mission and a study for BNSC on hyperspectral missions. Sira and Astrium would expect to bid in a common team to perform selected tasks in Phase A, if this proposal is successful, and would hope to share some of the mission development beyond Phase A.

5.2 Requirements for Data from Other Sources

6 References

Antyufeev, V. S., and Marshak, A. L., 1990, Inversion of monte-carlo model for estimating vegetation canopy parameters. *Remote Sensing of Environment*, **33**, 201–209.

Asner, G., 1998, Biophysical and biochemical sources of variability in canopy reflectance. *Remote Sensing of Environment*, **64**, 234–253.

Baret, F., and Guyot, G., 1991, Potentials and limits of vegetation indices for LAI and APAR assessment. *Remote Sensing of Environment*, **35**, 161–173.

Barnsley, M., Lewis, P., O'Dwyer, S., Disney, M., Hobson, P., Cutter, M., and Lobb, D., 2000, On the potential of CHRIS/PROBA for estimating vegetation canopy properties from space. *Remote Sensing Reviews*, **19**, 171–189.

Barnsley, M. J., 1994, Environmental monitoring using multiple-view-angle (MVA) remotely-sensed data, In *Environmental remote sensing from global to regional scales*, edited by G. M. Foody, and P. J. Curran (Chichester: John Wiley and Sons), pp. 181–201.

Barnsley, M. J., and Allison, D., 1996, Effect of image-to-image misregistration on multiple-view-angle (MVA) data sets, In *Remote Sensing : Science and Industry, Proceedings of the 22nd Annual Conference of the Remote Sensing Society* (Nottingham: Remote Sensing Society), pp. 489–496.

Barnsley, M. J., Allison, D., and Lewis, P., 1997a, On the information content of multiple view angle (MVA) images. *International Journal of Remote Sensing*, **18**, 1937–1960.

Barnsley, M. J., Barr, S. L., and Tsang, T., 1997b, The production of land cover maps from satellite sensor images: Scaling issues and generalization techniques, In *Scaling up*, edited by P. van Gardingen, G. M. Foody, and P. J. Curran (Cambridge: Cambridge University Press), pp. 173–200.

Barnsley, M. J., Lewis, P., Sutherland, M., and Muller, J., 1997c, Estimating land surface albedo in the HAPEX-Sahel southern super- site: inversion of two BRDF models against multiple angle ASAS images. *Journal of Hydrology*, **189**, 749–778.

Barton, C., and North, P., 2001, Remote sensing of canopy light use efficiency using the photochemical reflectance index: Model and sensitivity analysis. *Remote Sensing of Environment*, **78**, 264–273.

Begue, A., and Myneni, R., 1996, Operational relationships between NOAA-Advanced Very High-Resolution Radiometer vegetation indexes and daily fraction of absorbed photosynthetically active radiation, established for Sahelian vegetation canopies. *Journal of Geophysical Research-Atmospheres*, **101**, 21275–21289.

Boochs, F., Kupfer, G., Dockter, K., and Kuhbauch, W., 1990, Shape of the red-edge as a vitality indicator for plants. *International Journal of Remote Sensing*, **11**, 1741–1753.

Bounoua, L., Collatz, G., Sellers, P., Randall, D., Dazlich, D., Los, S., Berry, J., Fung, I., Tucker, C., Field, C., and Jensen, T., 1999, Interactions between vegetation and climate: Radiative and physiological effects of doubled atmospheric CO_2. *Journal of Climate*, **12**, 309–324.

Cayrol, P., Kergoat, L., Moulin, S., Dedieu, G., and Chehbouni, A., 2000, Calibrating a coupled SVAT-vegetation growth model with remotely sensed reflectance and surface temperature — A case study for the HAPEX-Sahel grassland sites. *Journal of Applied Meteorology*, **39**, 2452–2472.

Charney, J., Stone, P., and Quirk, W., 1975, Drought in the Sahara: A biogeophysical feedback mechanism. *Science*, **187**, 434–435.

Claussen, M., and Gayler, V., 1998, The greening of the Sahara during the mid-Holocene: Results of an interactive atmosphere-biome model. *Global Ecology and Biogeography Letters*, **6**, 369–377.

Cox, P., Betts, R., Bunton, C., Essery, R., Rowntree, P., and Smith, J., 1999, The impact of new land surface physics on the GCM simulation of climate and climate sensitivity. *Climate Dynamics*, **16**, 183–203.

Cox, P., Betts, R., Jones, C., Spall, S., and Totterdell, I., 2000, Acceleration of global warming due to carbon-cycle feedbacks in a coupled climate model. *Nature*, **408**, 184–187.

Cox, P., Huntingford, C., and Harding, R., 1998, A canopy conductance and photosynthesis model for use in a GCM land surface scheme. *Journal of Hydrology*, **212–213**, 79–94.

Curran, P. J., Dungan, J. L., Macler, B. A., Plummer, S. E., and Peterson, D. L., 1992, Reflectance spectroscopy of fresh whole leaves for the estimation of chemical concentration. *Remote Sensing of Environment*, **42**, 153.

Curran, P. J., Windham, W. R., and Gholz, H. L., 1995, Exploring the relationship between reflectance red edge and chlorophyll concentration in slash pine leaves. *Tree Physiology*, **15**, 203–206.

Decolstoun, E. C. B., Walthall, C. L., Russell, C. A., and Irons, J. R., 1995, Estimating the fraction of absorbed photosynthetically active radiation (fAPAR) at FIFE with airborne bidirectional spectral reflectance data. *Journal of Geophysical Research-Atmospheres*, **100**, 25523–25535.

Defries, R., Field, C., Fung, I., Justice, C., Los, S., Matson, P., Matthews, E., Mooney, H., Potter, C., Prentice, K., Sellers, P., Townshend, J., Tucker, C., Ustin, S., and Vitousek, P., 1995, Mapping the land-surface for global atmosphere-biosphere models — toward continuous distributions of vegetations functional-properties. *Journal of Geophysical Research-Atmospheres*, **100**, 20867–20882.

Delworth, T., and Manabe, S., 1993, Climate variability and land-surface processes. *Advances in Water Resources*, 3–20.

Deschamps, P.-Y., Bréon, F. M., Leroy, M., Podaire, A., Bricaud, A., Buriez, J. C., and Seze, G., 1994, The POLDER mission — instrument characteristics and scientific objectives. *IEEE Transactions on Geoscience and Remote Sensing*, **32**, 598–615.

Dickinson, R., Shaikh, M., Bryant, R., and Graumlich, L., 1998, Interactive canopies for a climate model. *Journal of Climate*, **11**, 2823–2836.

Diner, D. J., Beckert, J. C., Reilly, T. H., Ackerman, T. P., Bruegge, C. J., Conel, J. E., Davies, R., Gerstl, S. A. W., Gordon, H. R., Kahn, R. A., Martonchik, J. V., Muller, J.-P., Myneni, R., Pinty, B., Sellers, P. J., and Verstraete, M. M., 1998, Multi-angle Imaging SpectroRadiometer (MISR): instrument description and experiment overview. *IEEE Transactions on Geoscience and Remote Sensing*, **36**, 1500–1530.

Filella, I., and Peñuelas, J., 1994, The red edge position and shape as indicators of plant chlorophyll content, biomass and hydric status. *International Journal of Remote Sensing*, **15**, 1459–1470.

Flowerdew, R. J., and Haigh, J. D., 1997, Retrieving land surface reflectances using the ATSR-2: A theoretical study. *Journal of Geophysical Research-Atmospheres*, **102**, 17163–17171.

Foley, J., Kutzbach, J., Coe, M., and Levis, S., 1994, Feedbacks between climate and boreal forests during the Holocene epoch. *Nature*, **371**, 52–54.

Friedlingstein, P., Bopp, L., Ciais, P., Dufresne, J.-L., Fairhead, L., LeTreut, H., Monfray, P., and Orr, J., 2001, Positive feedback between future climate change and the carbon cycle. *Geophysical Research Letters*.

Gao, W., and Lesht, B. M., 1997, Model inversion of satellite-measured reflectances for obtaining surface biophysical and bidirectional reflectance characteristics of grassland. *Remote Sensing of Environment*, **59**, 461–471.

Goel, N. S., 1987, Models of vegetation canopy reflectance and their use in the estimation of biophysical parameters from reflectance data. *Remote Sensing Reviews*, **3**, 1–212.

Goel, N. S., 1989, Inversion of canopy reflectance models for estimation of biophysical parameters from reflectance data, In *Theory and applications of optical remote sensing*, edited by G. Asrar (New York: John Wiley and Sons), pp. 205–251.

Goel, N. S., Qin, W. H., and Wang, B. Q., 1997, On the estimation of leaf size and crown geometry for tree canopies from hotspot observations. *Journal of Geophysical Research-Atmospheres*, **102**, 29543–29554.

Holben, B., Kimes, D., and Fraser, R. S., 1986, Directional reflectance response in AVHRR red and near-IR bands for 3 cover types and varying atmospheric conditions. *Remote Sensing of Environment*, **19**, 213–236.

Ichoku, C., and Karnieli, A., 1996, A review of mixture modelling techniques for sub-pixel land cover estimation. *Remote Sensing Reviews*, **13**, 161–186.

IPCC, 2001, Climate Change 2001: The Scientific Basis. Summary for Policymakers, Technical report, Intergovernmental Panel on Climate Change, 55p.

Justice, C. O., Vermote, E., Townshend, J. R. G., Defries, R., Roy, D. P., Hall, D. K., Salomonson, V. V., Privette, J. L., Riggs, G., Strahler, A. H., Lucht, W., Myneni, R. B., Knyazikhin, Y., Running, S. W., Nemani, R. R., Wan, Z. M., Huete, A. R., Vanleeuwen, W., Wolfe, R., Giglio, L., Muller, J. P., Lewis, P., and Barnsley, M. J., 1998, The Moderate Resolution Imaging Spectroradiometer (MODIS): land remote sensing for global change research. *IEEE Transactions On Geoscience and Remote Sensing*, **36**, 1228–1249.

Kaufman, Y. J., and Tanré, D., 1992, Atmospherically resistant vegetation index (ARVI) for EOS-MODIS. *IEEE Transactions on Geoscience and Remote Sensing*, **30**, 261–270.

Knorr, W., and Heimann, M., 2001, Uncertainties in global terrestrial biosphere modeling. Part I: A comprehensive sensitivity analysis with a new photosynthesis and energy balance scheme. *Global Biogeochemical Cycles*, **15**, 207–225.

Knorr, W., and Schulz, J.-P., 2001, Using satellite data assimilation to infer global soil moisture status and vegetation feedback to climate, In *Remote Sensing and Climate Modelling: Synergies and Limitations*, edited by M. Benitson, and M. Verstraete, Advances in Global Change Research (Dordrecht and Berlin: Kluwer Academic Publishers), pp. 273–306.

Koster, R., Suarez, M., and Heiser, M., 2000, Variance and predictability of precipitation at seasonal-to-interannual timescales. *Journal of Hydrometeorology*, **1**, 26–46.

Leese, J., 2001, Coordinated Enhanced Observing Period (CEOP) Implementation Plan, Technical Report IGPO Publication Series No 36, GEWEX/WCRP, Silver Spring, Maryland, USA.

Leeuwen, W. J. D. v., Huete, A. R., Duncan, J., and Franklin, J., 1994, Radiative-transfer in shrub savanna sites in Niger — preliminary results from HAPEX-Sahel. 3: Optical-dynamics and vegetation index sensitivity to biomass and plant cover. *Agricultural and Forest Meteorology*, **69**, 267–288.

Los, S., Collatz, G., Bounoua, L., Sellers, P., and Tucker, C., 2001, Global interannual variations in sea-surface temperature, land-surface vegetation, air temperature, and precipitation. *Journal of Climate*, 1535–1549.

Los, S., Collatz, G., Sellers, P., Malmström, C., Pollack, N., DeFries, R., Bounoua, L., Parris, M., Tucker, C., and Dazlich, D., 2000, A global 9-year biophysical land-surface data set from NAOAA AVHRR data. *Journal of Hydrometeorology*, **1**, 183–199.

Lucht, W., Schaaf, C., and Strahler, A., 2000, An algorithm for the retrieval of albedo from space using semiempirical BRDF models. *IEEE Transactions on Geoscience and Remote Sensing*, **38**, 977–998.

Matthews, E., 1983, Global vegetation and land-use: new high resolution data-bases for climate studies. *Journal of Climatology and Applied Meteorology*, **22**, 474–487.

Moellering, H., and Tobler, W., 1972, Geographical variances. *Geographical Analysis*, **4**, 34–64.

Myneni, R., Maggion, S., Iaquinto, J., Privette, J., Gobron, N., Pinty, B., Kimes, D., Verstraete, M., and Williams, D., 1995, Optical remote-sensing of vegetation — modeling, caveats, and algorithms. *Remote Sensing of Environment*, **51**, 169–188.

Myneni, R., and Williams, D., 1994, On the relationship between FAPAR and NDVI. *Remote Sensing of Environment*, **49**, 200–211.

Nicodemus, F., Richmond, J., Hsia, J., Ginsberg, I., and Limperis, T., 1977, Geometrical Considerations and Nomenclature for Reflectance, Technical Report NBS Monograph 160, Institute for Basic Standards, Washington, D.C., USA.

North, P., Briggs, S., Plummer, S., and Settle, J., 1999, Retrieval of land surface bidirectional reflectance and aerosol opacity from ATSR-2 multi-angle imagery. *IEEE Transactions on Geoscience and Remote Sensing*, **37**, 526–537.

O'Neill, R., DeAngelis, D., Waide, J., and Allen, T., 1986, *A Hierarchical Concept of Ecosystems* (Princeton, New Jersey: Princeton University Press).

Otto-Bleisner, B., and Upchurch, G., 1997, Vegetation-induced warming of high latitude regions during the Late Cretaceous period. *Nature*, **385**.

Parry, M., 2000, Climate change: where should our priorities be? *Global environmental change*, **11**, 257–260.

Peñuelas, J., Filella, I., Biel, C., Serrano, L., and Savé, R., 1993, The reflectance at the 950–970 nm region as an indicator of plant water status. *International Journal of Remote Sensing*, **14**, 1887–1905.

Peñuelas, J., Filella, I., Serrano, L., and Savé, R., 1996, Cell wall elasticity and water index (R970 nm/R900 nm) in wheat under different nitrogen availabilities. *International Journal of Remote Sensing*, **17**, 373–382.

Pinar, A., and Curran, P. J., 1996, Grass chlorophyll and the reflectance red edge. *International Journal of Remote Sensing*, **17**, 351–357.

Pinty, B., and Verstraete, M. M., 1992, On the design and validation of surface bidirectional reflectance and albedo models. *Remote Sensing of Environment*, **41**, 155–167.

Polcher, J., 1995, Sensitivity of tropical convection to land-surface processes. *Journal of the Atmospheric Sciences*, **52**, 3143–3161.

Potter, C., Randerson, J., Field, C., Matson, P., Vitousek, P., Mooney, H., and Klooster, S., 1993, Terrestrial ecosystem production: A process model based on global satellite data. *Global Biogeochemical Cycles*, **7**, 811–841.

Privette, J. L., Emery, W. J., and Schimel, D. S., 1996a, Inversion of a vegetation reflectance model with NOAA AVHRR data. *Remote Sensing of Environment*, **58**, 187–200.

Privette, J. L., Myneni, R. B., Emery, W. J., and Hall, F. G., 1996b, Optimal sampling conditions for estimating grassland parameters via reflectance model inversions. *IEEE Transactions on Geoscience and Remote Sensing*, **34**, 272–284.

Qi, J., Chehbouni, A., Huete, A. R., and Kerr, Y. H., 1994, A modified soil adjusted vegetation index. *Remote Sensing of Environment*, **48**, 119–126.

Qiu, J., Gao, W., and Lesht, B. M., 1998, Inverting optical reflectance to estimate surface properties of vegetation canopies. *International Journal of Remote Sensing*, **19**, 641–656.

Roujean, J.-L., and Bréon, F. M., 1995, Estimating PAR absorbed by vegetation from bidirectional reflectance measurements. *Remote Sensing of Environment*, **51**, 375–384.

Roujean, J.-L., Leroy, M., and Deschamps, P. Y., 1992, A bidirectional reflectance model of the Earth's surface for the correction of remote-sensing data. *Journal of Geophysical Research-Atmospheres*, **97**, 20455–20468.

Roujean, J.-L., Tanré, D., Bréon, F. M., and Deuze, J. L., 1997, Retrieval of land surface parameters from airborne POLDER bidirectional reflectance distribution function during HAPEX-Sahel. *Journal of Geophysical Research-Atmospheres*, **102**, 11201–11218.

Sellers, P., 1986, Simple biosphere model (SiB) for use within general circulation models. *Journal of Atmospheric Science*, **43**, 505–531.

Sellers, P., Los, S., Justice, C., Dazlich, D., Collatz, G., and Randall, D., 1996, A revised land surface parameterization (SiB-2) for atmospheric GCMs. Part 2: The generation of global fields of terrestrial biophysical parameters from satellite data. *Journal of Climate*, **9**, 706–737.

Strahler, A. H., Lucht, T., W., Barker-Schaaf, C., Tsang, T., Gao, F., Li, X., Muller, J.-P., Lewis, P., and Barnsley, M., 1999, MODIS BRDF/Albedo Product: Algorithm Theoretical Basis Document Version 5.0, Technical Report Version 5.0, NASA, EOS-MODIS, GSFC, Maryland, USA.

Taylor, C., and Lebel, T., 1998, Observational evidence of persistent convective-scale rainfall patterns. *Monthly Weather Review*, **126**, 1597–1607.

Townshend, J. R. G., and Justice, C. O., 1988, Selecting the spatial-resolution of satellite sensors required for global monitoring of land transformations. *International Journal of Remote Sensing*, **9**, 187–236.

Verhoef, W., 2000, Simultaneous retrieval of soil, leaf, canopy and atmospheric parameters from hyperspectral information in the red-edge through model inversion, Technical Report NLR-TP-2000-126, National Aerospace Laboratory, 11pp.

Verstraete, M., Pinty, B., and Myneni, R., 1996, Potential and limitations of information extraction on the terrestrial biosphere from satellite remote-sensing. *Remote Sensing of Environment*, **58**, 201–214.

Waltershea, E. A., Blad, B. L., Hays, C. J., Mesarch, M., Deering, D. W., and Middleton, E. M., 1992, Biophysical properties affecting vegetative canopy reflectance and absorbed photosynthetically active radiation at the FIFE site. *Journal of Geophysical Research-Atmospheres*, **97**, 18925–18934.

Waltershea, E. A., Privette, J., Cornell, D., Mesarch, M. A., and Hays, C. J., 1997, Relations between directional spectral vegetation indices and leaf area and absorbed radiation in alfalfa. *Remote Sensing of Environment*, **61**, 162–177.

Wanner, W., Li, X., and Strahler, A. H., 1995, On the derivation of kernels for kernel-driven models of bidirectional reflectance. *Journal of Geophysical Research-Atmospheres*, **100**, 21077–21089.

Wanner, W., Strahler, A. H., Hu, B., Lewis, P., Muller, J. P., Li, X., Schaaf, C. L. B., and Barnsley, M. J., 1997, Global retrieval of bidirectional reflectance and albedo over land from EOS MODIS and MISR data: theory and algorithm. *Journal of Geophysical Research-Atmospheres*, **102**, 17143–17161.

Weins, J., 1989, Spatial scaling in ecology. *Functional Ecology*, **3**, 385–397.

Wu, Y. C., and Strahler, A. H., 1994, Remote estimation of crown size, stand density, and biomass on the oregon transect. *Ecological Applications*, **4**, 299–312.

Xue, Y., and Shukla, J., 1993, The influence of land-surface properties on Sahel climate. 1. Desertification. *Journal Of Climate*, **6**, 2232–2245.

Zeng, N., and Neelin, J., 2000, The role of vegetation-climate interaction and interannual variability in shaping the African Savanna. *Journal of Climate*, **13**, 2665–2670.

Zeng, N., Neelin, J., Lau, W.-M., and Tucker, C., 1999, Enhancement of interdecadal climate variability in the Sahel by vegetation interaction. *Science*, **286**, 1537–1540.

Annex: Team Composition

Lead-Investigator — Prof. Michael John Barnsley

Resumé

Prof. Barnsley has 19 years of research experience in the fields of remote sensing (Earth Observation) and Geographical Information Systems. His specialisms include: (i) the estimation of land-surface biophysical and biochemical properties by inverting multiple-view-angle image data against numerical models of surface radiation scattering; (ii) the analysis of vegetation biodiversity using hyperspectral image data; and (iii) mapping and monitoring urban areas in very high spatial resolution image data using structural pattern recognition techniques. He has published extensively in each of these areas. He is a lead member of several current satellite-sensor missions, notably CHRIS/PROBA (ESA/BNSC), SPOT-4 VGT (CNES) and Terra-1 MODIS (NASA). He set up and now leads the Environmental Modelling and Earth Observation (EMEO) research group at the University of Wales Swansea, which currently consists of five full-time academics, four post-doctoral research officers and a large body of post-graduate research students.

Personal Details

Name:	Barnsley, Michael John
Date of birth:	9th June 1960
Nationality:	British
Post:	Research Professor of Remote Sensing & GIS and Deputy Head of Department
Employer:	University of Wales Swansea
Address:	Department of Geography, Singleton Park, Swansea SA2 8PP, U.K.
Telephone:	01792-295647 (UK), +44-1792-295647 (International)
Fax:	01792-295955 (UK), +44-1792-295955 (International)
Email:	m.barnsley@swansea.ac.uk
URL:	http://stress.swan.ac.uk/mbarnsle/

Employment

1995–present	Research Professor of Remote Sensing and GIS, Department of Geography, University of Wales Swansea.
1989–1995	Lecturer in Remote Sensing and GIS / Director, University of London Remote Sensing Unit, Department of Geography, University College London.
1984–1989	'New Blood' Lecturer in Remote Sensing & GIS, post held jointly between the Departments of Geography, Birkbeck College and University College London.

BIOSphere-ATmosphere interaction mission/Pointable Hyperspectral Imager (BIOSAT/PHI)

Research Projects

1. Awarded a total of £2m in reseach grants since 1988 by the Natural Environment Research Council (NERC), Economic and Social Research Council (ESRC), BNSC, CNES and others.

2. Current research projects:

   a) Deriving estimates of land surface albedo, LAI and fAPAR from a novel, pointable, compact, high-resolution imaging spectrometer and physically-based models of vegetation canopy reflectance

   b) Mobilisation and transportation of metal in the Lower Swansea Valley: a post-industrial urban regeneration zone.

   c) Mapping and monitoring urban land use and morphology using satellite remote sensing and GIS.

   d) Estimating land surface biophysical properties using satellite remote sensing and crop growth models.

3. Recently completed research projects include:

   a) Development of a region-based, graph-theoretic spatial modelling and analysis system.

   b) Determination and validation of land-surface biophysical properties using SPOT-4 VEG-ETATION and HRVIR.

   c) Global and regional topography and vegetation cover for hydrological modelling.

   d) Improved determination of albedo and surface roughness at multiple spatial scales using remotely-sensed data and physical models of surface scattering for HAPEX- Sahel.

   e) Land surface processes for climate modelling using AVHRR, ATSR and MODIS.

Membership of Scientific Committees

1997–present	Member, NERC Earth Observation Expert Group.
1996–present	Member, Ordnance Survey (OS) Science and Technology Advisory Group, .
1996–2000	Member, British National Space Centre Earth Observation Programme Board.
1997–present	Member, British National Space Centre LINK Programme Board.
1995–1999	Chairman, NERC Airborne Remote Sensing Facility Steering Committee.
1996–1997	Member, NERC Earth Observation Programme Board.
1995–1997	Member, NERC Earth Observation Research Grants and Training Awards Committee.

Involvement in International Satellite Sensor Missions

1999–present	Land Science Leader, CHRIS/PROBA mission (SIRA/BNSC/ESA)
1997–2000	Principal Investigator, SPOT-4 Vegetation (CNES)
1995–1997	Principal Investigator, POLDER on ADEOS (CNES/NASDA)
1989–present	Associate Investigator, MODIS Science Team (NASA)

University of Wales Swansea

Environmental Modelling and Earth Observation (EMEO) Group

The EMEO group is one of five research groups within the Department of Geography at the University of Wales Swansea. Set up in 1996 and led by Prof. Barnsley, the group now consists of five full-time academic staff (Prof. Mike Barnsley, Dr. Sietse Los, Dr. Adrian Luckman, Dr. Peter North and Mr. Paul Pan) with expertise in optical and microwave remote sensing, radiative-transfer modelling, digital image processing (notably structural pattern-recognition techniques and SAR interferometry), environmental modelling and Geographical Information Systems. The group currently employs four full-time post-doctoral research officers and has a large body of post-graduate research students.

Members of the EMEO research group have active research links to a number of current international satellite-sensor programmes, including CHRIS/PROBA (Barnsley and North), Terra-1 MODIS (Barnsley), NOAA-AVHRR (Los), ERS-1/2 ATSR (North), SPOT-4 VGT (Barnsley and North), and ENVISAT ASAR (Luckman), in many instances playing a lead role in the design and implementation of these missions. The group has also been invited to bid for recognition as a Centre of Excellence in Earth Observation by the UK's Natural Environment Research Council (NERC). The bid, which is led by Swansea is being made in conjunction with, among others, colleagues from the Joint Centre for Hydro-Meteorological Research (JCHMR) at the Centre for Ecology and Hydrology (CEH) Wallingford (Dr. Richard Harding), and the Hadley Centre for Climate Prediction and Research (Dr. Peter Cox).

The EMEO group has extensive, dedicated data-processing and field data collection facilities, including a networked cluster of high-specification servers and workstations, with over 1TB of online disk storage. This is soon to be augmented with a new 20-processor Beowulf cluster and 3TB of RAID disk storage.

The BIOSAT Science Team

Name and Affiliation	Area of Expertise *(Involvement in other missions)*
Dr. Sietse Los Department of Geography University of Wales Swansea, UK	Global vegetation dynamics; IGBP programme
Dr. Jorg Kaduk Department of Geography, University of Leicester, UK	Carbon cycle modelling

Dr. Richard Harding Joint Centre for Hydro-Meteorological Research, Centre for Ecology and Hydrology, Wallingford, UK	Land surface schemes in Global Climate Models
Dr. Wolfgang Lucht	BRDF model inversion Dynamic vegetation models *MODIS*
Dr. Philip Lewis Department of Geography, University College London, UK	BRDF modelling and inversion *MODIS, SPOT-VGT, CHRIS/PROBA*
Dr. Peter North Department of Geography, University of Wales Swansea, UK	BRDF model inversion Atmospheric correction *ATSR, SPOT-VGT, CHRIS/PROBA*
Dr. Jim Collatz	Plant physiology
Dr. Jeff Privette NASA GSFC, Maryland, USA	BRDF model inversion CEOS validation programme *MODIS, MISR and VIIRS*
Dr. Axel Kleidon Department of Geography, University of Maryland, USA	Data assimilation
Dr. Stephane Jacquemoud Laboratoire Environnement et Développement Universite Paris 7 — Denis Diderot, Paris, France	Hyperspectral data analysis BRDF model inversion
Dr. Han Dolman	Surface radiation fluxes
Dr. Stephan Sandmeier	BRDF measurement
Prof. Jan-Peter Muller Department of Geomatic Engineering, University College London	Geomatic data processing *MODIS and MISR*

SIRA Electro-Optics Ltd

Sira Electro-Optics Ltd is a UK company with a heritage extending over the last 25 years of supplying space-based instrumentation for a range of platforms, both European and US. Sira's particular strengths lie in the ability to supply optical systems for Earth observation and pointing sensor requirements.

Sira Electro-Optics Ltd has a particularly strong reputation in the supply of innovative solutions and instrumentation for Earth observation missions. Earth observation missions for which Sira Electro-Optics Ltd has had particular involvement include MERIS, GOMOS, Medium Wave Infrared Imager for STRV2 and more recently the CHRIS instrument shortly to be flown on PROBA.

A full description of Sira Electro-Optics Ltd's space and other capability is provided on the web site `http://www.siraeo.co.uk`.

Astrium

The Astrium group is Europe's largest space company, able to act as prime contractor and provide complete space-based systems for communications, scientific and Earth Observation applications, including satellites, their control facilities, and all the necessary ground infrastructure to support them. Astrium Ltd is UK based, and forms part of Astrium's Earth Observation and Science directorate.

Astrium also supplies platforms for numerous scientific, Earth Observation and commercial satellite projects, and has outstanding experience of interfacing with numerous payload instruments. Astrium supplied or is supplying the platform for all the members of the SPOT, Olympus, Helios, ERS, Envisat, Metop, Rosetta, Mars Express, ECS and Eurostar series of programmes.

Astrium EU has a strong heritage in spacecraft programmes particularly in advanced high performance GNC, structures and thermal subsystems. This experience will provide BIOSAT with up to date experience of the technology required to fulfil the mission requirements.

Astrium Ltd has worked directly with strategic partners such as Sira Electro-Optics for several years in the definition of hyperspectral missions and related design, algorithm, and data processing issues. The following studies have contributed to our experience of hyperspectral missions:

- Advanced Microsatellite Mission for ESA;

- Hyperspectral Imaging Study in collaboration with Sira Electro-Optics for the BNSC ATS programme;

- Advanced Avionics Study for the BNSC ATS programme;

- Study of a Hyperspectral Mission for Biochemical / Biophysical Assessments in collaboration with Sira Electro-Optics and University of Wales Swansea for the BNSC Newton programme BNSC Newton; and

- The advanced methods for lossless compression of hyperspectral data in collaboration with MDA for ESA.

Advanced High Performance AOCS

Astrium Ltd. was responsible for the advanced AOCS on the following recent scientific programmes: SOHO, Cluster, XMM, and Integral, and will be responsible for the AOCS system on ADM if the Astrium Ltd. is selected as the prime contractor.

Figure 16: XMM AOCS System under test.

The XMM AOCS subsystem has performed extremely well since launch, all the performance requirements are met or exceeded, and XMM is now the most accurately pointed spacecraft ever produced in Europe.

The integral flight model AOCS subsystem was delivered to Alenia in June 1999. Since that time, the flight performance analysis has been completed and delivered together with a range of supporting study notes. As with all previous Astrium UK AOCS subsystems, the integral system has been demonstrated to be fully compliant with all performance requirements under worst-case conditions.

Advanced Structures

Astrium Ltd. capability in the design, development, manufacture and test of advanced lightweight structures includes CFRP and Kevlar skins/cores and laminates. Astrium Ltd. has the full suite of structural design and analysis software. Thick-skinned CFRP monocoque technology has been qualified under BNSC funding. Over thirty six satellite structures, fifty SPELDA structures for Ariane 4, ACU 1663 and ASAP5 adaptors for Ariane 5, METOP Service Module and the Dual Launch Adaptor for Delta II have been manufactured at Stevenage within the past 15 years.

A full description of Astrium Ltd's heritage is provided on the web site `http://www.astrium-space.com/`.
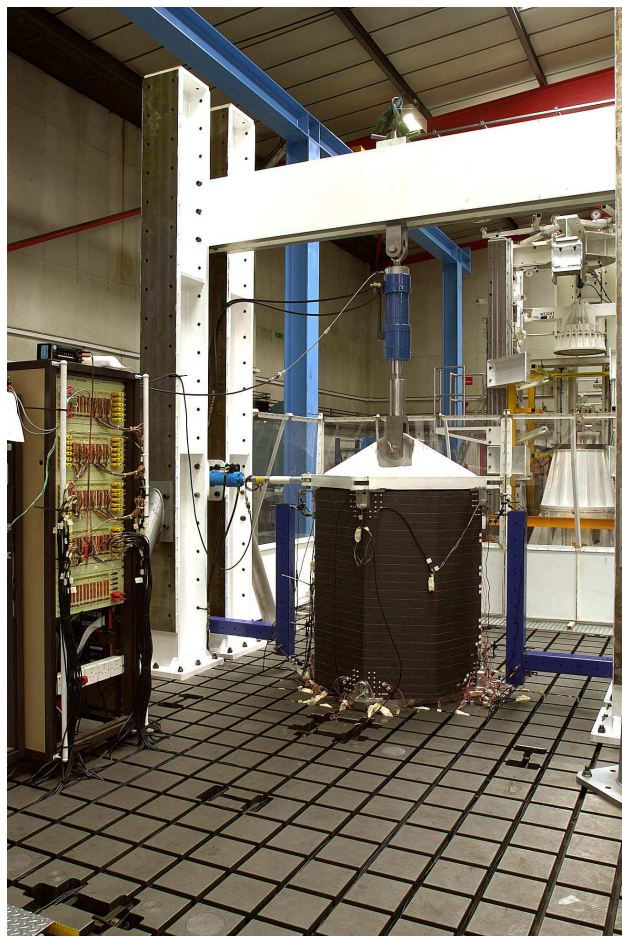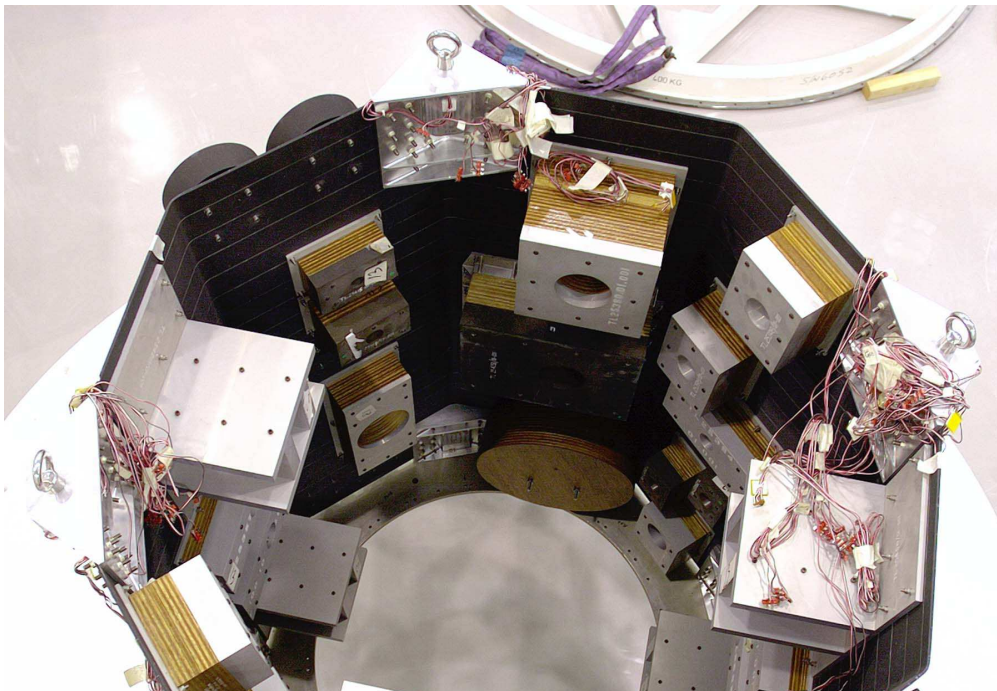
Figure 17: Filament wound structure equipped with mass dummies for sine test (top) and undergoing static test (bottom).